Article:
Salem, M., Basoalto-Ibarra, H., Espadero Sanchez-Crespo, M. et al. (2026) A Physics-based investigation of solidification morphology and microcracking in a high-γ Ni-based superalloy during Selective Laser Melting. Acta Materialia, 311. 122170. ISSN: 1359-6454

https://doi.org/10.1016/j.actamat.2026.122170

A Physics-Based Investigation of Solidification Morphology and Microcracking in a High-γ' Ni-Based Superalloy During Selective Laser Melting

Mostafa Salem[a,b,*] Hector Basoalto[b], Miguel Espadero[b], Hugh Banes[2], Prashant Jadhav[b], Yu Lu[c]

[a] Advanced Metallic Systems Centre for Doctoral Training, University of Sheffield, Sheffield, UK

[b] Department of Materials Science and Engineering, University of Sheffield, Sheffield, UK

[c] Department of Materials Science and Engineering, University of Birmingham, Birmingham, UK

*Corresponding author: msalem2@sheffield.ac.uk

Graphical Abstract

A Physics-Based Investigation of Solidification Morphology and Microcracking in a High-γ' Ni-Based Superalloy During Selective Laser Melting

Mostafa Salem, Hector Basoalto, Miguel Espadero, Hugh Banes, Prashant Jadhav, Yu Lu

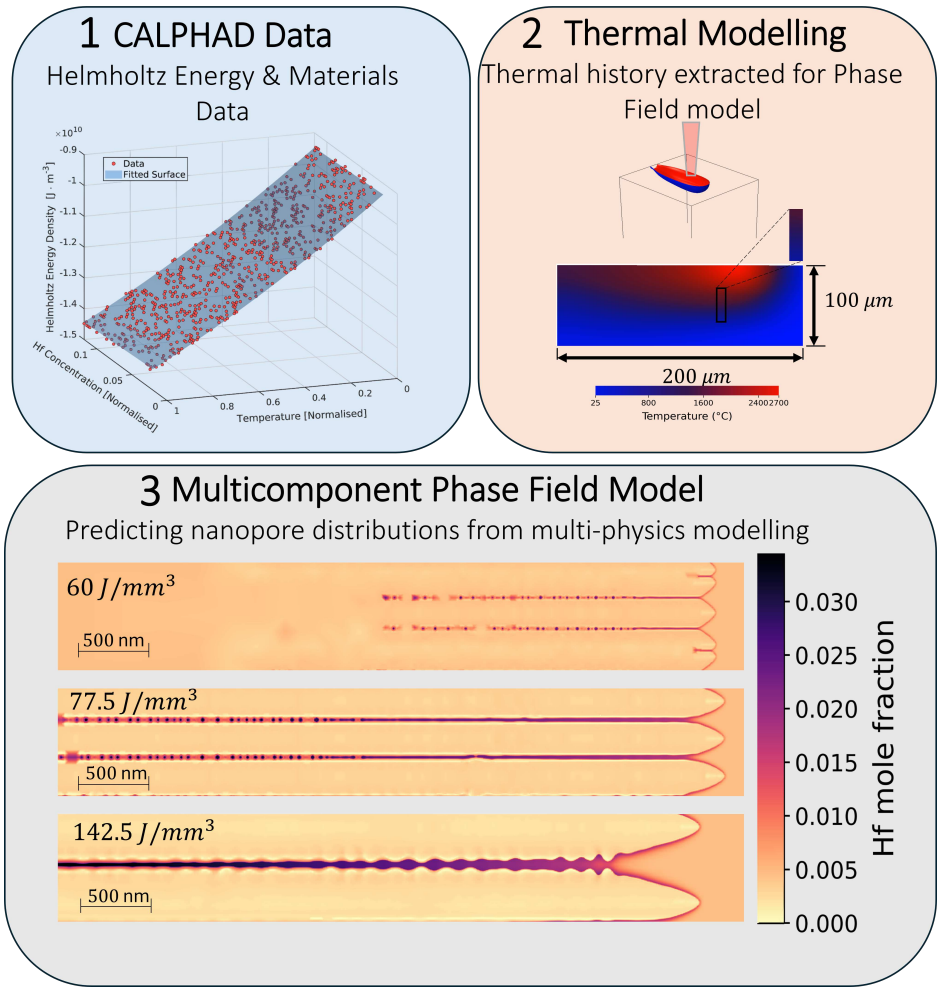

Highlights

A Physics-Based Investigation of Solidification Morphology and Microcracking in a High-γ' Ni-Based Superalloy During Selective Laser Melting

Mostafa Salem, Hector Basoalto, Miguel Espadero, Hugh Banes, Prashant Jadhav, Yu Lu

- Thermal data extracted at the melt pool's fusion boundary was used to define phase-field solidification conditions in CM247LC under selective laser melting.
- The phase-field model predicts the transition from cellular to dendritic solidification as a function of local thermal history and energy density.
- Optical and SEM observations link dendritic microstructures to increased nanovoid clustering and microcracking, despite reduced lack-of-fusion porosity.
- The study explains why reducing lack-of-fusion porosity by increasing energy density in CM247LC inherently promotes cracking.
- The results indicate that process design should focus on controlling heat distribution and exposure to control the thermal gradient and cooling rate experienced by the system.

A Physics-Based Investigation of Solidification Morphology and Microcracking in a High-γ' Ni-Based Superalloy During Selective Laser Melting

Mostafa Salem[a,b,*], Hector Basoalto[b], Miguel Espadero[b], Hugh Banes[b], Prashant Jadhav[b], Yu Lu[c]

[a] *University of Sheffield, Advanced Metallic Systems Centre for Doctoral Training, UK*

[b] *University of Sheffield, Department of Materials Science and Engineering, UK*

[c] *University of Birmingham, Department of Materials Science and Engineering, UK*

Abstract

This work employs a computational approach to investigate how local thermal conditions and dendritic growth angles influence the solidification morphology of the difficult-to-print Ni-based superalloy CM247LC during Selective Laser Melting (SLM). A conduction-based thermal model incorporating temperature-dependent material properties was used to extract local thermal gradients and cooling rates under single-track laser conditions. These thermal histories were then used as input to a multicomponent phase-field model to simulate the evolution of the solidification front, including nanovoid formation and elemental segregation. This framework enables the simulation of location-specific solidification morphologies and microsegregation under SLM conditions.

Model predictions were validated through comparison with SEM and optical microscopy, revealing a direct correlation between dendrite development, nanovoid size distribution, and microcracking propensity. Based on these results, a microc-

*Corresponding author. Email address: msalem2@sheffield.ac.uk

racking mechanism is proposed in which nanovoids form within interdendritic regions during solidification and subsequently coalesce to form microcracks. Once calibrated against thermodynamic data, the phase-field model was used to examine how processing parameters govern the transition between cellular and dendritic growth. The results demonstrate that reducing lack-of-fusion porosity requires a transition to dendritic solidification, which in turn promotes microcracking in CM247LC. These findings indicate that the fabrication of crack-free and porosity-free components requires a processing window that achieves sufficient melting while maintaining cooling rates that favour a cellular microstructure.

Keywords:
Additive Manufacturing, Selective Laser Melting, Multiphysics, Solidification, Phase-Field

---

1. Introduction

Selective Laser Melting (SLM) has emerged as a disruptive technology that manufacturing industries are attempting to capitalise on [1]. SLM works by melting neighbouring tracks of powder using a focused laser beam, which is repeated on successive layers until a part is finally consolidated. A near-net-shape component is therefore produced, making it ideal for applications where raw material is expensive, difficult to mechanically work, or where only low production volumes are required [2]. As a result, the potential to print Ni-based Superalloys has aroused interest in the aerospace, power, and nuclear sectors [3].

Nickel-based Superalloys possess excellent material properties at elevated temperatures, which makes them attractive for use in the hot end of powerplants and gas turbine engines [4]. However, the exceptionally high yield strength of these alloys makes them difficult to machine or form, even at high temperatures [5]. Printing these alloys using SLM has been largely successful for weldable compositions, such as Inconel 718 or Inconel 625, which feature a low volume fraction of γ' [6]. Printing alloys with a high fraction of γ' remains challenging due to their microc-

racking propensity [1, 5]. A particular example of this is the printing of CM247, which is a popular casting alloy in aerospace. Part of the challenge in printing these high-γ' alloys is that the cracking mechanism is not well understood [7]. The two prominent theories of cracking in high-γ' alloys are Ductility Dip Cracking (DDC), which postulates that the ductility reduction at intermediate temperatures (0.2 - 0.7 of melting) causes failure at the grain boundaries [6, 8]; and liquation cracking, which associates the cracking with a large freezing range for high-γ' alloys [9]. Carter et al. suggested that the cracking of CM247 [8] resulted from DDC; whereas Vrancken et al. [10] dismissed DDC as a major cause of cracking. The latter cited the need for MC carbides for the DDC failure mechanism, while the high cooling rate that is characteristic of SLM does not allow enough time for MC carbides to precipitate substantially. Recently, Tang et al. [11] showed that three distinct crack morphologies are present in CM247LC, which points to the presence of all three mechanisms: solidification cracking, liquation cracking, and DDC.

From a numerical perspective, efforts to explain crack formation in high-γ' Ni-based superalloys under SLM conditions remain limited. Existing modelling studies have largely focused on melt pool behaviour or macroscopic porosity, without explicitly resolving solidification morphology or nanoscale defect formation. For example, Basoalto et al. [12] showed that CM247LC exhibits a higher pore density than Inconel 718 based on melt pool simulations alone, but did not consider solidification mechanisms. More recent efforts by Lindroos et al. [13] and Pinomaa et al. [14] have coupled phase-field and crystal plasticity approaches to study dislocation evolution during rapid solidification. However, these studies did not address solidification porosity or cracking, and the alloys considered were unrelated to Ni-based superalloys. As a result, a physics-based, location-resolved description linking local solidification conditions to defect formation and cracking in high-γ' alloys is still lacking.

In light of this gap, the present work investigates the origin of microcracking in CM247LC during SLM by explicitly modelling solidification morphology and

nanoscale porosity formation. A computational framework is developed in which finite element thermal simulations provide local thermal gradients and cooling rates at the fusion boundary, which are then used as input to a multicomponent phase-field model calibrated to CALPHAD thermodynamics. This approach enables direct simulation of location-specific solidification morphologies, solute segregation, and the formation of trapped liquid pockets within intercellular and interdendritic regions. Based on the large solidification shrinkage strain of liquid Nickel, these trapped liquid regions are interpreted as nanovoids. By comparing predicted nanovoid distributions with experimentally observed porosity and microcracking, the results indicate that cracking in CM247LC is dominated by a solidification-driven mechanism involving nanovoid formation and coalescence. This conclusion is consistent with recent experimental observations by Templeton et al. [15] linking solidification morphology and cracking propensity.

In the context of solidification theory, hot cracking remains a primary mechanism for defect formation that limits the processability of advanced alloys. Despite decades of research, a universally effective cracking metric is still lacking, even in traditional casting [16]. Classical criteria often rely on significant simplifications; for example, the Clyne-Davies (CSC) model provides only qualitative indications [16], while the Rappaz-Drezet-Gremaud (RDG) model treats interdendritic pressure drop as a constant, neglecting local microstructural variations [17].

Recent phase-field (PF) studies sought to address these limitations. For instance, Wang et al. [18] established important phenomenological links between microstructural patterns and cracking in binary Al-Cu welding, demonstrating that susceptibility relates to the length of liquid channels and the entrapment of liquid pockets. Their findings suggest that cellular morphologies with isolated liquid regions are more resistant to failure. The Integrated CFD-PF model by Chen et al. [17] showed that traditional RDG and Kou metrics can miscalculate interdendritic pressure drops by several orders of magnitude and fail to account for the critical influence of grain orientation [17]. Additionally, the work by Yang et al. [19] demonstrates that grain boundary properties have a great influence on sus-

ceptibility of the polycrystal to form cracks. Yang et al. [19] demonstrated this by varying the orientation of neighboring grains as well as the grain boundary energy and was able to calculate the expected pressure drop at the grain boundary using the RDP model. Importantly, the work by Yang et al. [19] and Chen et al. [17] focused on calculating cracking susceptibility metrics from the phase-field solutions, while Wang et al. [18] used a multi-scale approach to understand where in the melt pool cracks were most likely to be seen.

The present work builds upon these phenomenological principles mentioned in classical hot cracking works but extends the scope to the challenges of SLM. While earlier studies focused on binary systems and welding scales [18], this work utilizes a multicomponent phase-field framework to investigate high-γ' Ni-based superalloys. We link SLM processing conditions to dendritic morphology and, specifically, to the distribution of nanopores and microcracking observed experimentally. We do so quantitatively using a grand potential-based phase-field model with an asymptotically derived antitrapping current.

To the authors' knowledge, this work represents the first physics-based, multicomponent phase-field study of solidification morphology and nanoscale porosity formation in a high-γ' Ni-based superalloy under SLM conditions, and the first to directly link these solidification phenomena to experimentally observed microcracking.

2. Methodology

2.1. Experimental Techniques

Five samples of CM247LC were fabricated on the Aconity Lab with energy densities of 45 $J \cdot mm^{-3}$, 60 $J \cdot mm^{-3}$, 65 $J \cdot mm^{-3}$, 77.5 $J \cdot mm^{-3}$, and 142.5 $J \cdot mm^{-3}$. The manufactured specimens consisted of 10 mm $\times$ 10 mm $\times$ 10 mm solid cuboids. The composition of the CM247LC powder is shown in Table 1. The specific machine parameters remain proprietary and are not shared in this paper.

For all the manufactured samples in this work, a constant layer height of $20\mu m$ was used.

Table 1: The composition of the CM247LC alloy used in this paper.

Element	Al	Co	Cr	Hf	Mo	Ta	Ti	W	Zr
Composition [%]	5.6	9.2	8.1	1.4	0.5	3.2	0.7	9.5	0.015

Optical microscopy was used to observe the porosity and microcracks in the samples. Scanning Electron Microscopy (SEM) was then used in the BSE mode to observe elemental segregation. The SEM analysis was done with a JEOL JSM-7000F microscope.

2.2. Phase-Field Modelling

This work adopts the grand-potential phase-field model of Aagesen et al. [20], which is capable of handling multiple phases and crystallographic orientations. This work implemented a CALPHAD approach to incorporate the influence of temperature and composition into the grand potential energy function. Since only solidification is considered here, the framework reduces to two phases — solid and liquid - each with their respective order parameter. The model is described briefly in this section, and an asymptotic analysis following Choudhury et al. [21] was performed to derive the antitrapping current; full details are given in Appendix D.

The phase-field method relies on explicitly defining an energy functional that captures the relevant physics of the problem. There are three components to the energy functional in the case of the grand potential-based phase-field method. The energy functional for this method includes an interface component ω_{int}, a multi-well energy component ω_{mw}, and a thermodynamic component ω_{th}. These contributions are shown in the integrand in Equation 1.

$$\Omega = \int_V \omega_{int} + \omega_{mw} + \omega_{th} dV \tag{1}$$

The interfacial energy per unit volume (ω_{int}) is defined using the square of the gradient operator as shown in Equation 2. More specifically, the total interfacial energy is given by the sum over interfacial energies of all phases present at that point. This is shown in Equation 2, where the factor κ is calculated to maintain a constant interfacial energy compared with the sharp-interface case. Note that the letters α and β in the subscripts of all equations in this paper are used to denote different phases. The symbols i and j in the subscripts represent the different grain orientations. $\eta_{\alpha i}$ is therefore the phase fraction of grains with orientation i consisting of phase α.

$$\omega_{int} = \frac{\kappa}{2} \sum_{\alpha=1}^{N} \sum_{i=1}^{p_\alpha} |\nabla \eta_{\alpha i}|^2 \tag{2}$$

The next component of the energy functional is the multi-well energy density (ω_{mw}), which as the name indicates, represents energy minima where the phase fractions $\eta_{\alpha i}$ equal either one or zero, respectively. For a binary system, the multi-well energy density reduces to a double-well function where the minima are at zero and one. When the phase fractions deviate from their multi-well values the energy of the system increases, which provides an inhibiting force against phase transitions. This multi-well energy density is given by the following expression.

$$\omega_{mw} = \sum_{\alpha=1}^{N} \sum_{i=1}^{p_\alpha} \left(\frac{\eta_{\alpha i}^4}{4} - \frac{\eta_{\alpha i}^2}{2}\right) + \sum_{\alpha=1}^{N} \sum_{i=1}^{p_\alpha} \sum_{\beta=1}^{N} \sum_{j=1, \alpha i \neq \beta j}^{p_\beta} \frac{\Upsilon_{\alpha i \beta j}(\theta)}{2} \eta_{\alpha i}^2 \eta_{\beta j}^2 + \frac{1}{4} \tag{3}$$

It should be noted that this model includes anisotropy in the form of $\Upsilon_{\alpha i \beta j}(\theta)$ term in Equation 4. Notice that $\Upsilon_{\alpha i \beta j}(\theta)$ is a dimensionless parameter that influences the multiwell energy barrier and is equal to $\frac{3}{2}$ for an isotropic interface. δ is the strength of anisotropy, θ is the direction of the normal to the surface at a point, and θ_0 is the reference angle for the anisotropic growth. The factor k is equal to four for cubic systems and six for HCP crystals. Importantly, this model by

Aagesen et al. [20] includes the anisotropy in the cross-bulk term rather than in interfacial energy term. It can be shown, however, that this formulation returns the Gibbs-Thomson relation in the thin-interface limit and is therefore valid for modelling anisotropic surfaces. The proof of this is included in Appendix E.

$$\Upsilon_{\alpha i \beta j}(\theta) = \bar{\Upsilon}_{\alpha i \beta j}\left[1 + \delta \cos\left(\frac{k}{2\pi}(\theta - \theta_0)\right)\right] \tag{4}$$

The components of the phase-field energy functional described above are essentially multi-order extensions of the well-studied WBM, KKS, and Kobayashi models [22, 23, 24]. More importantly, in the case of the aforementioned models, the Helmholtz energy of the solid and liquid phases is used to construct ω_{th}. In this study, the grand potential is used to construct the thermodynamic contribution ω_{th} since it allows multiple species to be included in the energy definition without having an excessive number of conditions enforcing equality of the chemical potentials [1]. As shown in Equation 5, ω_{th} is calculated as a weighted sum over the grand potential of the individual phases ω_α. $h_{\alpha i}$ represents a switching function that lies between zero and one. The switching function used in this work is shown in Equation 6.

$$\omega_{th} = \sum_{\alpha=1}^{N} \omega_\alpha \sum_{i=1}^{p_\alpha} h_{\alpha i} \tag{5}$$

$$h_{\alpha i} = \frac{\eta_{\alpha i}^2}{\sum_{\beta=1}^{N} \sum_{i=1}^{p_\alpha} \eta_{\beta i}^2} \tag{6}$$

The grand potential is calculated for each component using the expression in Equation 7, where f_α is the Helmholtz Energy Density, ρ_I is the molar density of the alloying element I and μ_I is the chemical potential of alloying element I.

[1] In the Kim-Kim-Suzuki model, for example, a proxy expression for chemical potential is enforced at every point.

Specifically, ρ_I is defined by Equation 8, where V_m is the molar volume.

$$\omega_\alpha = f_\alpha - \sum_{I=1}^{K-1} \rho_I \mu_I \tag{7}$$

$$\rho_I = \frac{c_I}{V_m} \tag{8}$$

So far, the equations describe only the system's energy; the dynamics still need to be defined. This is done using the Allen-Cahn equation, which dictates the evolution of the phase-field parameter $\eta_{\alpha i}$ and is given in Equation 9. In Equation 9, L is the Allen-Cahn mobility. The evolution of the alloying elements' concentration is given by Equation 10. The derivation of Equation 10 is detailed by Choudhury et al. [21] and begins with the Cahn-Hilliard equation $\frac{\partial c_I}{\partial t} = \nabla \cdot (M_{II} \nabla \frac{\delta F}{\delta c_I})$. χ_{II} is self-susceptibility of element I, which is defined by the partial derivative $\frac{\partial \rho_I}{\partial \mu_I}$. M_{II} represents the self-mobility of element I.

$$\frac{\partial \eta_{\alpha i}}{\partial t} = -L \frac{\delta \Omega}{\delta \eta_{\alpha i}} \tag{9}$$

$$\chi_{II} \frac{\partial \mu_I}{\partial t} - \nabla \cdot M_{II} \nabla \mu_I = -\sum_{\alpha=1}^{N} \sum_{i=1}^{p_\alpha} \frac{\partial \rho_I}{\partial \eta_{\alpha i}} \frac{\partial \eta_{\alpha i}}{\partial t} \tag{10}$$

The next step is to write an expression for the Helmholtz Energy Density. By representing the Helmholtz Energy Density of phase α as a quadratic expression we can determine phase-field properties analytically. This is shown in Equation 11, where f_α^0 is the minimum value of the Helmholtz Energy Density, k_b^I is the curvature of the paraboloid along the concentration axis and k_T^I is the curvature along the temperature axis. Similarly, $c_I^{\min}$ and $T_I^{\min}$ are the concentration and temperature where the minimum energy is found, respectively. Notice that the aforementioned parameters in Equation 11 are not calculated from first principles

but are determined by fitting to CALPHAD data.

$$f_\alpha = f_\alpha^0 + \sum_{I=0}^{K-1} \frac{1}{2} k_{b,\alpha}^I \left(c_I^\alpha - c_I^{\alpha,\min} \right)^2 + \sum_{I=0}^{K-1} \frac{1}{2} k_{T,\alpha}^I \left(T_I^\alpha - T_I^{\alpha,\min} \right)^2 \tag{11}$$

This analytical expression enables us to directly calculate the chemical potential μ_I and the susceptibility χ_{II}. For brevity, only the main results are quoted below. For the derivation of these expressions, the reader is referred to reference [20]. The chemical potential in Equation 12 is the derivative of Helmholtz Energy Density with respect to ρ_I^α. The susceptibility in Equation 14 is defined as the rate of change of the Helmholtz Energy Density with respect to the chemical potential. ρ_I^α is defined as the molar density of element I in phase α and is calculated similarly to ρ_I in Equation 8.

$$\mu_I^\alpha = V_m k_{b,\alpha}^I (c_I^\alpha - c_I^{\alpha,\min}) \tag{12}$$

$$\rho_I^\alpha = \frac{\mu_I^\alpha}{k_{b,\alpha}^I V_m^2} + \frac{c_I^{\alpha,\min}}{V_m} \tag{13}$$

$$\chi_{II}^\alpha = \frac{1}{k_{b,\alpha}^I V_m^2} \tag{14}$$

Finally, because of the diffuse nature of the interface, and because the diffusivity of the solid is much lower than that of the liquid, a significant concentration of solute is retained in the solid that should have been ejected into the liquid [25]. This is corrected using an antitrapping term, which promotes the movement of solute from the solid into the liquid. The antitrapping term is shown in Equation 15. $W(\rho_l^I - \rho_s^I)$ represents the amount of solute per unit area of the interface that must be ejected to mitigate this spurious solute trapping. The factor a, which will be referred to here as the antitrapping factor, was necessarily introduced by

Karma et al. [26] to enable matching the conservation equations in the phase-field method to a velocity-dependent Gibbs-Thomson condition. Echebarria et al. [27] then extended the asymptotic analysis by Karma et al. [26] to mimic a one-sided diffusion model.

$$\vec{J}_A^I = aW(\rho_l^I - \rho_s^I)\frac{\nabla\eta_{\alpha i}}{|\nabla\eta_{\alpha i}|}\frac{\partial\eta_{\alpha i}}{\partial t} \tag{15}$$

With the antitrapping flux $\vec{J}_A^I$, the conservation equation for the chemical potential is shown in Equation 17. Choudhury et al. [21] performed an asymptotic analysis on a grand potential-based phase-field model to derive the appropriate antitrapping factor. Their approach was adapted to the phase-field model proposed by Aagesen et al. [20], and the full derivation is provided in Appendix D. The resulting antitrapping factor is shown in Equation 16.

$$a(\eta) = \frac{1}{4\sqrt{2}}\frac{g(\eta)[1-h(\eta)]}{\eta(\eta-1)} \tag{16}$$

The antitrapping factor is then included in the chemical potential evolution equation to give Equation 17. Although Equation 17 is derived from the conservation equation, discretisation errors in the chemical potential violate mass conservation [25, 28].

$$\chi_{II}\frac{\partial\mu_I}{\partial t} - \nabla\cdot M_{II}\nabla\mu_I - \nabla\cdot\frac{aW}{V_m}(c_l^I - c_s^I)\frac{\nabla\eta_{\alpha i}}{|\nabla\eta_{\alpha i}|}\frac{\partial\eta_{\alpha i}}{\partial t} = -\sum_{\beta=1}^{2}\frac{\partial\rho_I}{\partial\eta_{\beta 1}}\frac{\partial\eta_{\beta 1}}{\partial t} \tag{17}$$

To enforce mass conservation strictly, Equation 18 is enforced in place of the chemical potential evolution equation. This requires the chemical potential to be calculated from the solute concentration at every timestep by inverting Equation 19.

$$\frac{\partial c_I}{\partial t} = \nabla[\cdot M_{II} V_m \nabla \mu_I] + \nabla \cdot [aW(c_l^I - c_s^I)\frac{\nabla \eta_{\alpha i}}{|\nabla \eta_{\alpha i}|}\frac{\partial \eta_{\alpha i}}{\partial t}] \tag{18}$$

$$c_I = \sum_{\alpha} h_\alpha \left(\frac{\mu_I}{k_{b,I}^{\alpha} V_m} + c_{\min,I}^{\alpha} \right) \tag{19}$$

To account for the influence of the thermal gradient $\frac{dT}{dy}$ and cooling rate R on columnar solidification, the temperature field is imposed using the expression given in Equation 20. Within the phase-field domain, this formulation assumes a locally constant thermal gradient $\frac{dT}{dy}$ and cooling rate R. This assumption is justified because the computational domain is orders of magnitude smaller than the melt pool and because the thermal history is extracted locally at the fusion boundary from a macroscopic thermal conduction model.

$$T(y,t) = T_0 + \frac{dT}{dy}(y - y_0) - R(t - t_0), \tag{20}$$

As a result, the imposed temperature field represents a location-specific solidification environment rather than a globally averaged condition. The parameters $\frac{dT}{dy}$ and R therefore vary with spatial position within the melt pool and between processing conditions, even though they are treated as constant over the phase-field domain. The reference temperature T_0, position y_0, and time t_0 define the local coordinate system of the simulation. Equation 20 further implies that temperature variations are resolved only along the build direction, consistent with the development of columnar microstructures. The thermal gradient $\frac{dT}{dy}$ and cooling rate R are obtained from a thermal conduction model incorporating temperature-dependent material properties, as described in Section 2.3.

2.3. Thermal Modelling

In order to obtain an estimate for the thermal gradient and cooling rate of the melt pool boundary, a Representative Volume Element (RVE) of a single line scan was

used, similar to the approach described in [29]. A laser was modelled travelling across the surface of the powder bed, with a tri-variate Gaussian formulation for the laser source term as follows:

$$E(x,y,z) = \frac{2\eta P}{\sigma_x \sigma_y \sigma_z \pi^{3/2}} \exp\left(-\frac{1}{2}\left(\frac{(x-\mu_x)^2}{\sigma_x^2} + \frac{(y-\mu_y)^2}{\sigma_y^2} + \frac{(z-\mu_z)^2}{\sigma_z^2}\right)\right) \quad (21)$$

Where (μ_x, μ_y, μ_z) is the position of the centre of the heat source, η is the laser absorption efficiency typically in the range of 30%-40% and P is the laser power. The beam spread along the x, y, z axes are represented by the parameters $\sigma_x, \sigma_y, \sigma_z$. This travelling source term, moving at a speed of v across the powder bed, was coupled to the finite element software ABAQUS [30]. In these simulations, it was assumed that the powder bed can be modelled as a homogenous block with the height of the layer of powder, and further that the properties of the fluid flow in the melt pool can be represented by a higher heat transfer coefficient of material above liquidus temperature. These assumptions were chosen to reduce computational cost of the simulation. The absorptivity was determined by calibrating the numerical melt pool width against single laser scan data.

3. Numerical Implementation

3.1. Phase-Field Model

An explicit expression for the Helmholtz Energy Density (HED) is required for the phase-field method. The HED was obtained from ThermoCalc [31] and fitted to the paraboloid expression in Equation 11. The composition of the CM247LC alloy used is shown in Table 1. To minimise the computational cost of the phase-field simulations, the alloy composition space was reduced to four solute elements: Hf, Ta, Ti, and W. These elements were selected because both the present experimental data and previous studies on additively manufactured CM247LC consistently report strong microsegregation for these species [11, 32, 33, 34]. In contrast,

cobalt and chromium are not consistently identified in microsegregation maps of CM247LC in the literature and are typically reported to exhibit comparatively uniform distributions at the solidification scale. As the objective of the phase-field model is to capture solute-driven morphological instability caused by elemental partitioning, elements with minimal reported segregation were excluded from the reduced-order model without loss of physical fidelity.

For illustration, the fitted HED surface for the liquid phase against temperature and hafnium composition is shown in Figure 1. Similar looking surface fits were obtained for the liquid and solid phases against compositions of the other constituents. The fit quality was observed to be acceptable, so evaluating a goodness-of-fit metric was considered unnecessary. The surfaces were generated by varying the concentration of the system at a given temperature and evaluating the resulting HED value. For each of the fitted energy surfaces, only the concentration of the respective element (Hf, Ta, Ti, or W) was varied together with the balancing element.

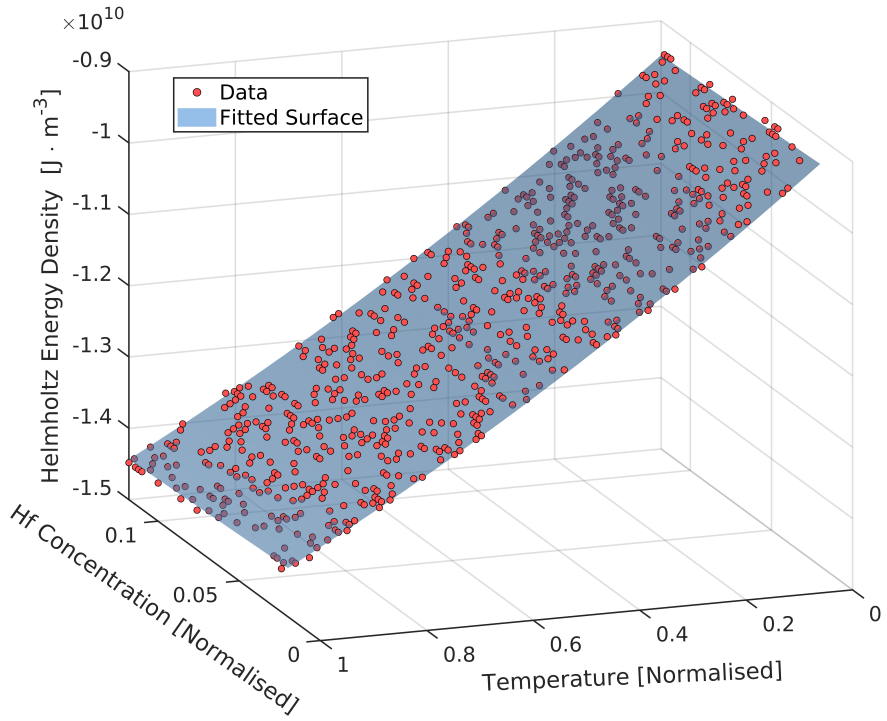

Figure 1: Helmholtz Energy Density (HED) plotted against normalised temperature and hafnium concentration, respectively. Five thousand data points were used to fit the surface in each case. A small selection of points is shown in this plot for the sake of clarity.

Although fits to the paraboloid surfaces were obtained, the multidimensionality of the composition space means that common tangents – in the pseudo-binary sense – do not exist. Unfortunately, this results in incorrect predictions of the equilibrium concentrations. To remedy this, a calibration procedure was followed whereby the energy curves at each temperature interval were translated such that the equilibrium concentrations at that temperature were equivalent to the equilibrium concentrations (in an isothermal sense). Figure 2(a) shows the solid and liquid surfaces before the calibration was performed. Figure 2(b) shows the curves projected by the respective surfaces onto the slicing plane shown in Figure 2(a). The corresponding surfaces and curves are shown in Figures 2(c)-(d). It should be noted that the calibrated HED surface is a paraboloid fit to the modified surface

in 2(a). This is an important consideration, because the surface will not fit the data exactly, meaning that for some temperatures – depending on the quality of the local fit – the composition's prediction will not be exactly correct. It is also important to note that the equilibrium composition will not always be achieved in a transient simulation because species take time to diffuse between the solid and the liquid.

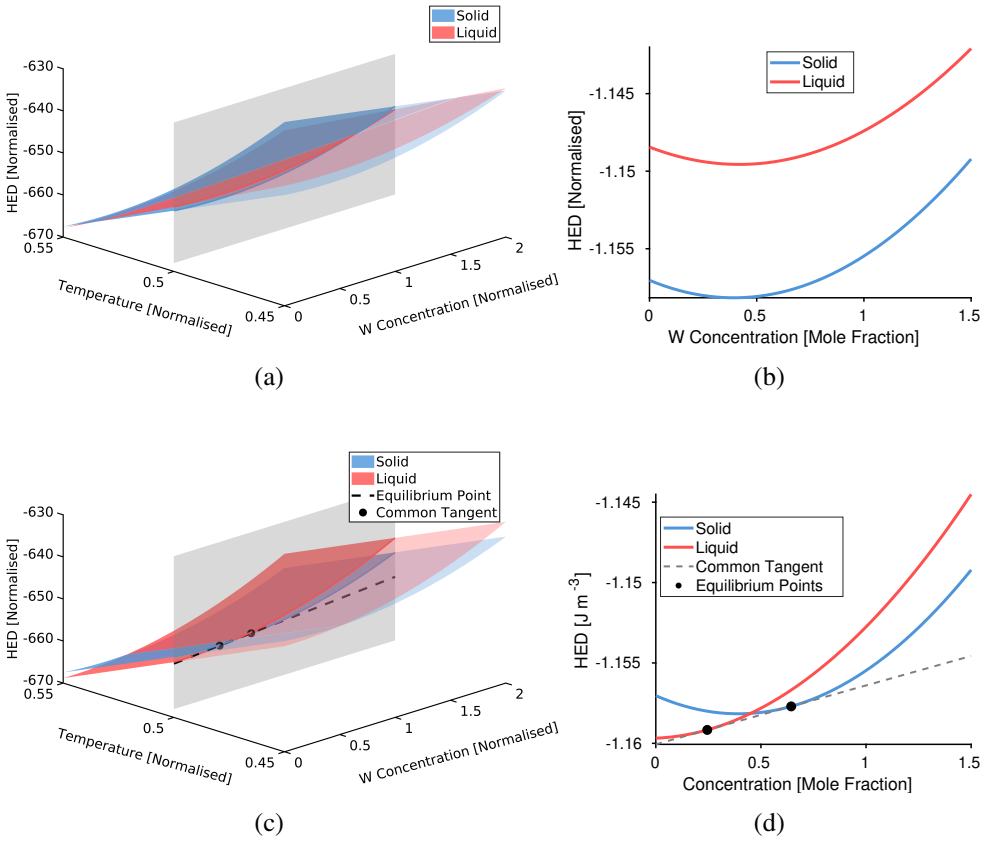

Figure 2: The calibration process to produce the correct equilibrium compositions at each temperature. The fitted HED surface prior to calibration is shown in (a), whereas the calibrated surface is shown in (c).

The dimensional parameters of the quadratic expressions for the solid and liquid phases, respectively, are shown in Table 2. The magnitude of the parameters is

very large, which will result in poorly conditioned matrices and therefore poor convergence. For brevity, the dimensional and normalised physical parameters used for simulating the solidification of CM247LC are provided in Appendix B along with the normalisation method.

Table 2: Parameters of the fitted paraboloid following the translation to match the equilibrium compositions, including additional terms for thermal properties.

	Solid Phase					Liquid Phase				
Element	$\mathbf{k^s_{b,I}}$ (J/m^3)	$\mathbf{c^s_{min,I}}$ (Mole Fraction)	$\mathbf{k^s_{T,I}}$ $(J/K/m^3)$	$\mathbf{T^s_{min}}$ (K)	$\mathbf{g^s_{min,I}}$ (J/m^3)	$\mathbf{k^l_{b,I}}$ (J/m^3)	$\mathbf{c^l_{min,I}}$ (Mole Fraction)	$\mathbf{k^l_{T,I}}$ $(J/K/m^3)$	$\mathbf{T^l_{min}}$ (K)	$\mathbf{g^l_{min,I}}$ (J/m^3)
Hf	1.30×10^{9}	3.44×10^{-2}	1.54×10^{7}	1.44×10^{5}	-6.48×10^{11}	1.15×10^{9}	5.48×10^{-2}	1.84×10^{9}	2.97×10^{3}	-1.94×10^{10}
Ta	5.94×10^{8}	6.12×10^{-2}	1.54×10^{7}	1.44×10^{5}	-6.48×10^{11}	6.29×10^{8}	6.02×10^{-2}	1.54×10^{7}	1.44×10^{5}	-6.49×10^{11}
Ti	7.15×10^{8}	4.82×10^{-2}	1.53×10^{7}	1.44×10^{5}	-6.51×10^{11}	7.27×10^{8}	5.09×10^{-2}	1.54×10^{7}	1.44×10^{5}	-6.49×10^{11}
W	1.31×10^{8}	1.98×10^{-2}	1.54×10^{7}	1.44×10^{5}	-6.49×10^{11}	1.31×10^{8}	6.01×10^{-2}	1.54×10^{7}	1.44×10^{5}	-6.54×10^{10}

3.2. Antitrapping Factor

3.2.1. Validation

Since composition has a strong effect on the growth morphology of dendrites, it was important to validate the antitrapping factor before proceeding with the simulations in this study. To do this efficiently, a one-dimensional non-linear solver was developed in Python to model the evolution of composition around a flat interface. A simple binary system was simulated using the phase-field formulation outlined in Section 2.2 under an isothermal condition. The material data for this binary system is shown in Table 3.

Table 3: The material data for a one-dimensional isothermal solidification simulation.

Property	k_s	k_l	c^s_{min}	c^l_{min}	f^s_{min}	f^l_{min}	D_s	D_l	c_0
Value	10	10	0.1	0.9	-0.1	0.1	1×10^{-5}	1	0.25

The concentration profile at steady-state was obtained with and without the antitrapping factor, and the result was compared against the analytical solution. This is shown in Figure 3, where the result without the antitrapping factor featured almost complete solute trapping. When the antitrapping factor was included, the concentration profile matched the analytical result. The analytical solution took

the form of the expression shown in Equation 22, where the interface velocity was approximated from the solution of the phase-field equations. In Equation 22, Δc is given by $(c^l_{\text{min}} - c_0)$ from Table 3.

$$c(x) = c_0 + \Delta c \exp\left(-\frac{v}{D_l}x\right) \tag{22}$$

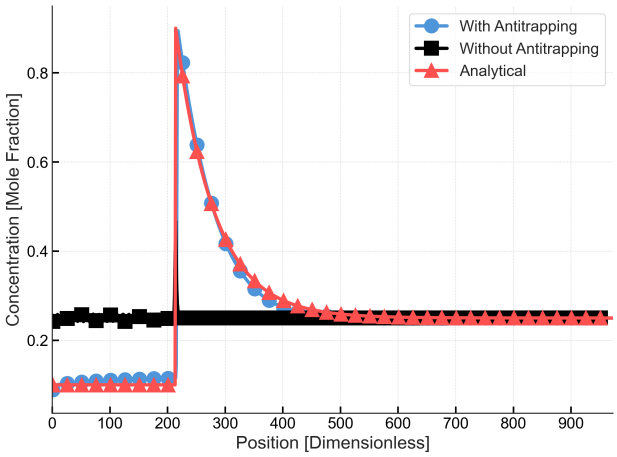

Figure 3: Concentration profile plots to validate the calculation of the antitrapping factor.

3.2.2. Justification of Classical Asymptotic Analysis

The asymptotic analysis used to calculate the antitrapping factor in this paper is based on the work of Choudhury et al. [21] and assumes equilibrium kinetics at the interface. This is justified because the velocity of the dendrites in this paper are much smaller than the diffusive velocity that is calculated by Aziz et al. [35] in deriving the Continuous Growth Model (CGM). The velocity of the dendrite tips are given in Table 4 for the five volumetric energy density (VED) cases investigated in this work. The diffusive velocity is calculated as shown in Equation 23. Taking the reported tracer diffusivity of the slowest-diffusing substitutional species (tungsten) in CM247LC, $D_L = 1.77 \times 10^{-9}$ m^{2}s^{-1} [31], and $\lambda = 2.63 \times 10^{-10}$ m [36] gives a conservative diffusive velocity $v_d = 6.7$ ms^{-1}. Since $v/v_d << 1$ in

Table 4, the partition coefficient given by CGM in Equation 24 is approximately equal to the equilibrium partition coefficient $k \approx k_e$.

Table 4: Dendritic growth velocities for each volumetric energy density (VED).

VED ($\mathrm{J\,mm^{-3}}$)	Interface velocity V ($\mathrm{m\,s^{-1}}$)	v/v_d ($v_d = 6.7\ \mathrm{m\,s^{-1}}$)
45	0.353	0.0527
60	0.226	0.0337
65	0.232	0.0346
77.5	0.141	0.0210
142.5	0.0746	0.0111

$$v_d = \frac{D_l}{\lambda} \tag{23}$$

$$k = \frac{k_e + v/v_d}{1 + v/v_d} \tag{24}$$

To further examine this approximation, we consider the most strongly segregating element in CM247LC, which is hafnium. Using the Thermocalc [31] database, the partition coefficient of hafnium ranges from 0.14 to 0.28. Using a liquid diffusivity of $D_l = 3.6 \times 10^{-9}$, $v/v_d = 0.0259$ for the highest interface velocity in Table 4. This would return an error for hafnium's partition coefficient ranging from 6 % to 13 %. Keeping in mind the inherent uncertainty in values generated from CALPHAD databases, this error is taken to be acceptable for this study [37, 38]. Errors in the partition coefficients of other components are much lower since their equilibrium partition coefficients are greater than hafnium's.

3.3. Nanovoid Identification

At the end of the simulation, the domain is below the solidus temperature, with the exception of regions located near the tips of the cellular or dendritic structures. Remaining entrapped liquid pockets within the solidified domain are identified using the OpenCV [39] library following the algorithm outlined in Appendix C.

These liquid pockets are assumed to evolve into nanovoids upon complete solidification as a consequence of solidification shrinkage and insufficient feeding at the interdendritic scale.

As an illustration, Figure 4(a) shows the simulated solidification microstructure, while Figure 4(b) highlights the identified entrapped liquid regions that are treated as nanovoids in the subsequent analysis.

(a)

(b)

Figure 4: The solidification microstructure in (a) and the identified nanovoids in (b).

3.4. Thermal Modelling

To implement the proposed RVE approach, as mentioned previously, the moving heat source term in equation 21 was coupled to the finite element software ABAQUS using a user subroutine. When constructing the simulation domain, the boundaries of the domain (outside the RVE) were fixed at a temperature T_{Sink}. To ensure that a smooth transition between the temperature of the RVE and T_{Sink} occurred, a dissipation region with a coarse mesh was implemented, that was removed for result analysis. Further, to retain a balance of accuracy and computational efficiency, a mesh was constructed with a fixed cell size of 1 μm for the simulations.

For accurate predictions of the melt pool dimensions, and thus the cooling rate and thermal gradient, it is also necessary to include temperature dependent thermophysical properties of the studied alloy. To obtain this, ThermoCalc software

[31] was used to give CALPHAD-based predictions for key properties such as thermal conductivity, for use in the model.

The domain of the mesh that was used for the analyses is illustrated in Figure 5, which highlights the respective size of the phase-field simulation domain compared with the thermal simulations. The thermal gradient and cooling rate are calculated within that solidification sub-domain.

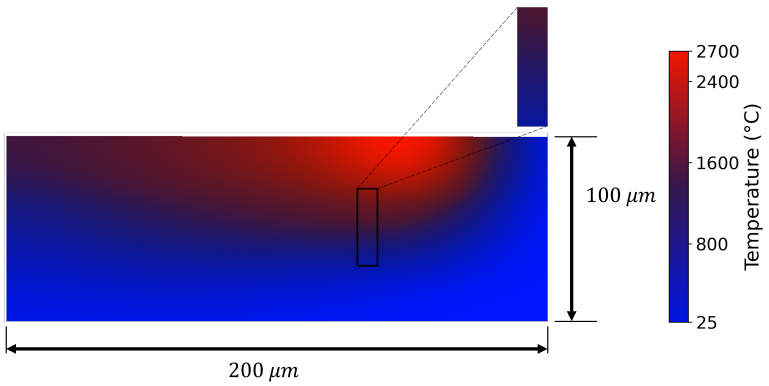

Figure 5: A cross-section of the conduction model at steady-state. The highlighted region of the melt pool illustrates the respective domain for the phase-field model, which is the region within which the average thermal gradient and cooling rate were determined.

4. Results

This study is comprised of three numerical investigations. The first explores the influence of energy density on solidification morphology and composition, with findings directly compared to experimental results. Next, a parametric study examines how thermal gradient and cooling rate impact the nanovoid size distribution, respectively. The simulation domain used in this work is depicted in Figure 6. Finally, the third study assesses the effect of dendrite/cell orientation on the nanovoid distribution. Throughout this paper, the term "growth angle" refers to the dendrites' orientation, as illustrated in Figure 6(b). It is important to note that, regardless of the growth angle, the thermal gradient is consistently assumed to be vertical, aligned with the build direction.

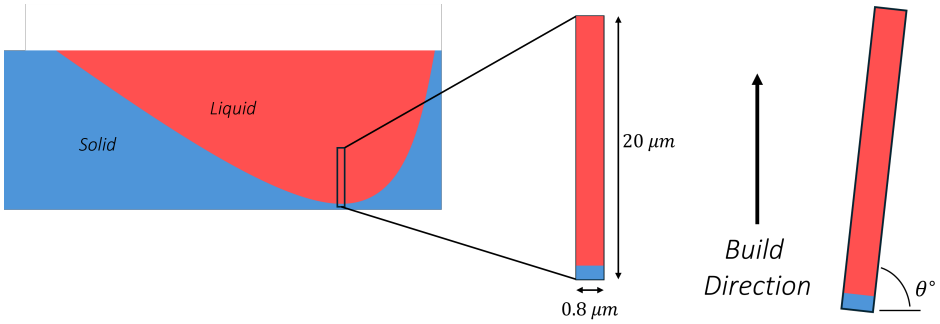

(a) Domain's Placement (b) Growth Angles

Figure 6: A schematic illustration showing the phase-field simulation domain's position with respect to the melt pool in (a). Definition of the reference growth angle θ_0 is illustrated in (b).

4.1. Energy Density

4.1.1. Solidification Morphology & Nanovoid Distributions

Five heat conduction simulations were performed with varying energy densities to evaluate the thermal gradient and cooling rate for the phase-field simulations. The corresponding values for each energy density are presented in Table 5.

Table 5: The thermal gradient and cooling rate extracted from each of the energy density simulations.

Energy Density $[J \cdot mm^{-3}]$	45	60	65	77.5	142.5
Thermal Gradient $[K \cdot m^{-1}]$	1.80×10^7	2.24×10^7	2.12×10^7	2.73×10^7	3.10×10^7
Cooling Rate $[K \cdot s^{-1}]$	6.94×10^6	5.25×10^6	5.15×10^6	3.91×10^6	2.30×10^6

The final solidification morphologies, observed after the dendrites fully extended across the domain (20 μm), are shown in Figure 8. As the energy density was increased from 45 to 142.5 $J \cdot mm^{-3}$, an increase in primary dendrite arm spacing (PDAS) is evident. This is attributed to both the increasing thermal gradient and the decreasing cooling rate as the energy density is raised. This is summarised in Table 5. Higher cooling rates raise the cut-off frequency for unstable interfacial perturbations, consistent with predictions from the Mullins–Sekerka interface stability theory [40], which is why more cells (and therefore a smaller PDAS) are

observed at lower energy densities. Moreover, this trend aligns with the empirical relationship reported by Harrison et al. [41], which describes PDAS as inversely proportional to a fractional power of the cooling rate.

Pores were identified using the OpenCV image analysis library [39], and their equivalent radii were calculated. The identification algorithm is briefly described in Appendix C. In this study, entrapped liquid pockets in the intercellular/interdendritic regions are assumed to develop into pores on freezing. Therefore, the remainder of this work will treat entrapped liquid pockets synonymously to nanovoids. The density change during the solidification of CM247LC was calculated with ThermoCalc to be 15 %, which is why this assumption is justified. Probability density curves of nanovoid radii, presented in Figure 7(a), along with the box plots in Figure 7(b), reveal that higher energy densities lead to an increase in both the average nanovoid radius and the interquartile range. The continuous probability density curves were calculated from the discrete pore distributions using a Kernel Density Estimate (KDE) method [42]. At 45 $J \cdot mm^{-3}$, the solidifying microstructure developed into a planar front with cellular caps and did not trap any nanovoids. Conversely, as can be seen in Figure 8(e), the 142.5 $J \cdot mm^{-3}$ case is dendritic and traps a long stable row of nanovoids behind the dendrites' tips.

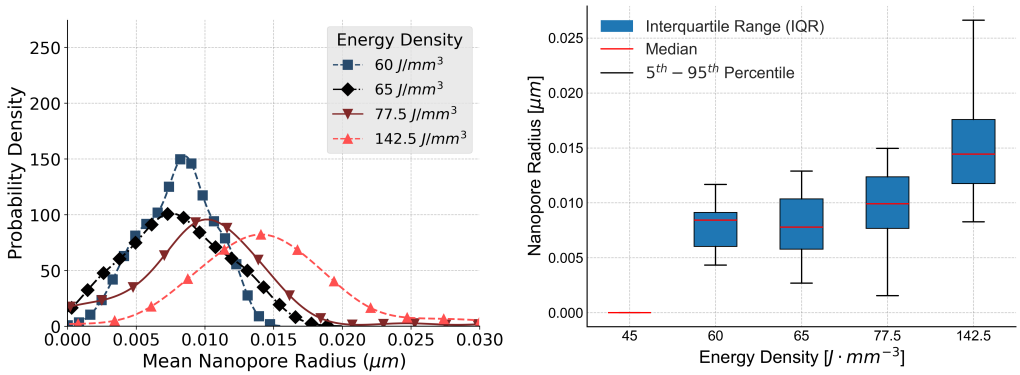

(a) (b)

Figure 7: A summary of the effect of changing the energy density on the distribution of nanovoids in the solidified domain. The probability density curves for the various energy densities are shown in (a). The effect on the median pore radius and interquartile range is captured in (b).

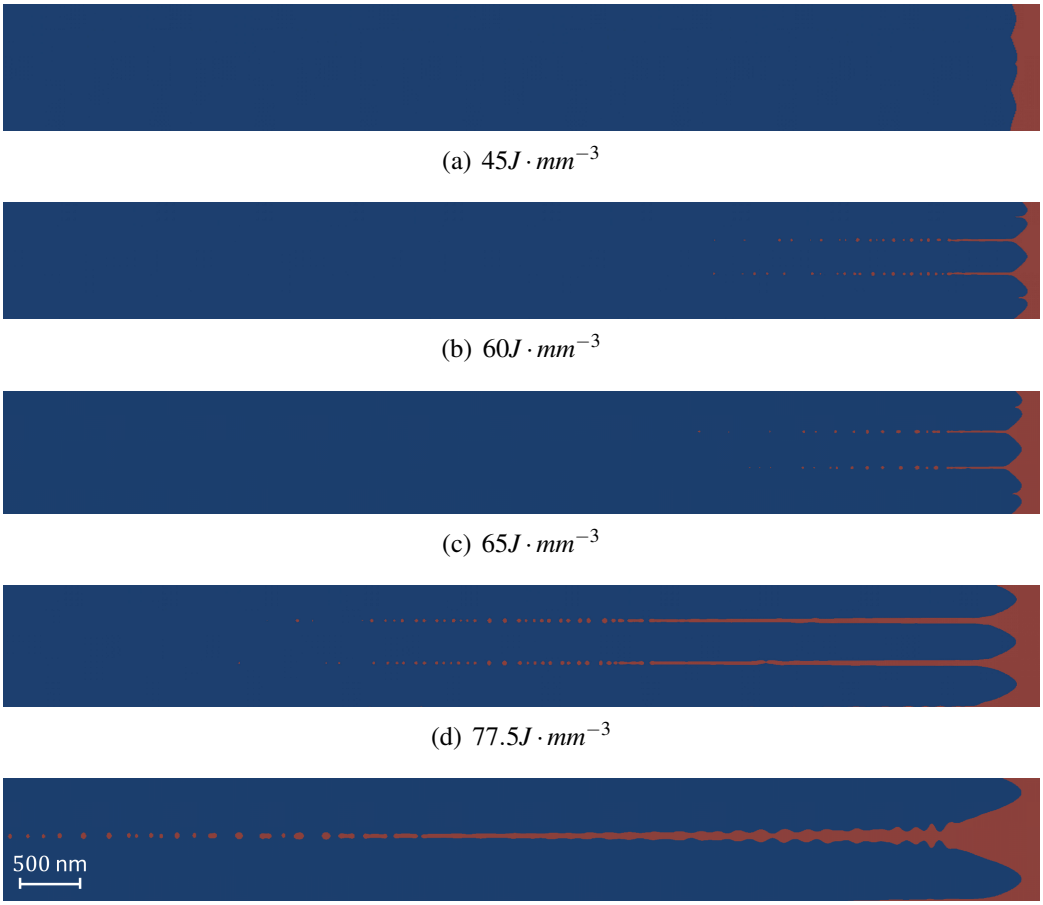

(a) $45J \cdot mm^{-3}$

(b) $60J \cdot mm^{-3}$

(c) $65J \cdot mm^{-3}$

(d) $77.5J \cdot mm^{-3}$

(e) $142.5J \cdot mm^{-3}$

Figure 8: Solidification pattern near the tip for the five energy densities investigated in this section. The blue regions are solid and the red ones are liquid. Only a quarter of the domain's length is shown for clarity.

The optical micrographs of the samples are shown in Figure 9. It is clear from the micrographs, due to the irregularity of the pores, that significant lack-of-fusion porosity is present and that it decreases with an increasing energy density. It is highlighted in Figure 10 that small microcracks begin to appear at 77.5 $J \cdot mm^{-3}$ and that these microcracks are considerably larger at the highest energy density case (142.5 $J \cdot mm^{-3}$). The reduction in lack-of-fusion porosity is expected with an increasing energy density since the powder is allowed to fully melt. The micro-

cracking can be explained by transition from cellular to dendritic microstructures as demonstrated in Figure 8 from the phase-field simulations. Further, this can be explained by the fact that a high cooling rate is obtained from entering the conduction zone [43].

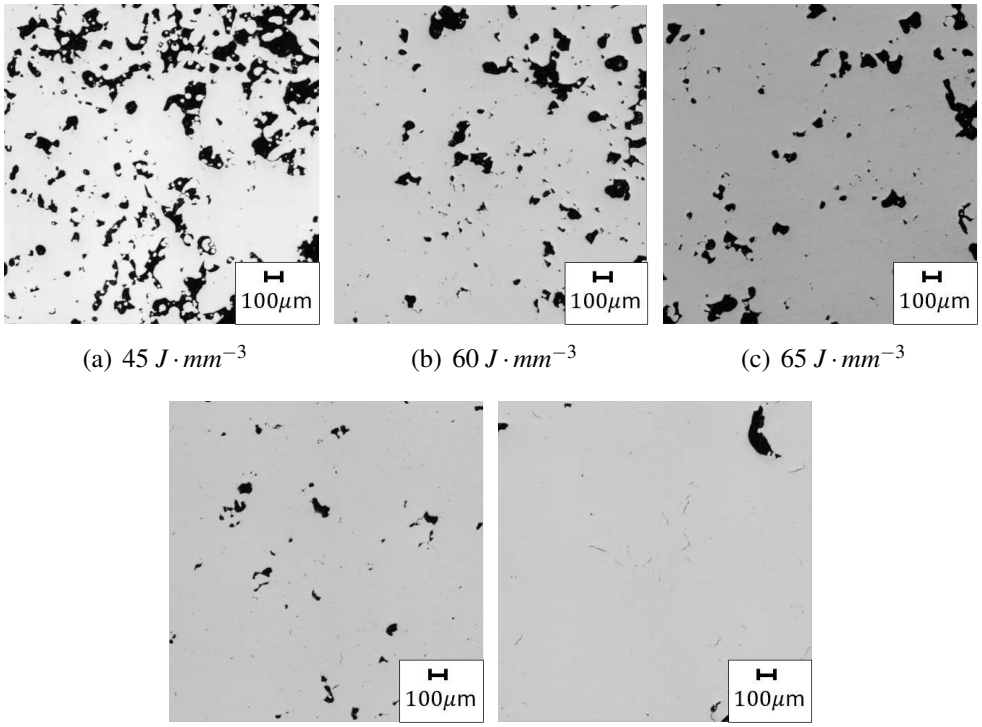

(a) 45 $J \cdot mm^{-3}$ (b) 60 $J \cdot mm^{-3}$ (c) 65 $J \cdot mm^{-3}$

(d) 77.5 $J \cdot mm^{-3}$ (e) 142.5 $J \cdot mm^{-3}$

Figure 9: Optical micrographs for the five investigated energy densities in the Transverse Direction (TD). The micrographs show decreasing lack-of-fusion porosity with increasing energy density. Lack-of-fusion porosity is still present, however, at the highest energy density.

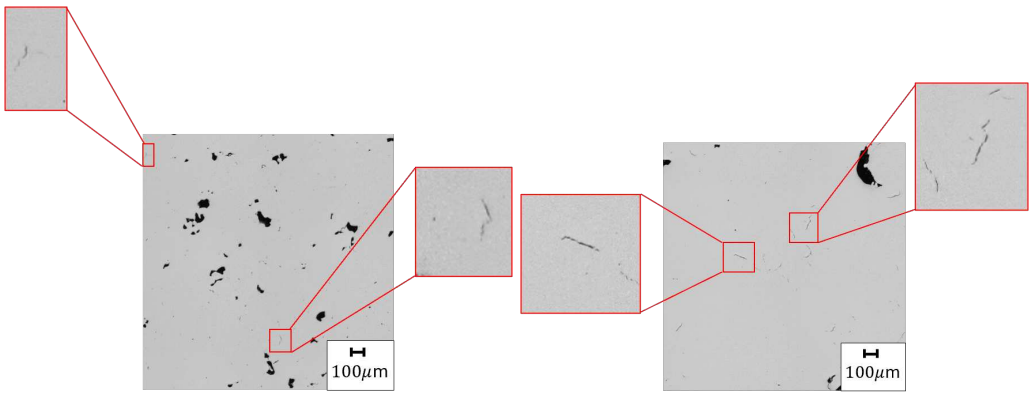

(a) 77.5 $J \cdot mm^{-3}$ (b) 142.5 $J \cdot mm^{-3}$

Figure 10: Highlighted regions showing microcracks in the two samples with the highest energy densities.

4.1.2. Microsegregation & SEM Evidence

The elemental concentrations of Hf, Ta, Ti, and W were predicted by the phase-field model. The degree of elemental segregation influences solid solution strengthening, as well as the freezing range of the alloy. By accurately predicting the degree of elemental segregation, Crystal Plasticity (CP) models can be supplied with spatio-temporal concentration data that would aid with microresidual stress predictions. This motivates the need for accurate phase-field simulations. This section, therefore reports the pattern of elemental segregation predicted by the phase-field model and compares it qualitatively to the SEM images taken in the Backscattered Electron (BSE) mode.

The phase-field results in Figure 11 show a marked increase in microsegregation as the energy density increases. The maximum percentage segregation is reached when the energy density is at 77.5 $J \cdot mm^{-3}$ and maintains that segregated composition at the energy density of 142.5 $J \cdot mm^{-3}$. The heatmaps only show the concentration of hafnium for brevity, but this pattern remains the same for the other alloying elements that are reported in Table 6. It is worth noting that the segregation in Table 6 is the maximum percentage segregation with respect to the

nominal composition and is calculated at 50 K below the solidus temperature. The percentage segregation was not extracted at the solidus temperature since non-equilibrium conditions delay complete solidification to lower temperatures. The expression for calculating the maximum percentage segregation is given in Equation 25. It is also worth noting that the maximum segregation observed at 77.5 $J \cdot mm^{-3}$ is similar to the composition reported by Fardan et al. [44] at grain boundaries using Atom Probe Tomography (APT). Fardan et al. reported a composition of Hf equal to 6 wt. % for an energy density of 75 $J \cdot mm^{-3}$, and the results in Table 6 report 7 wt. % for 77.5 $J \cdot mm^{-3}$.

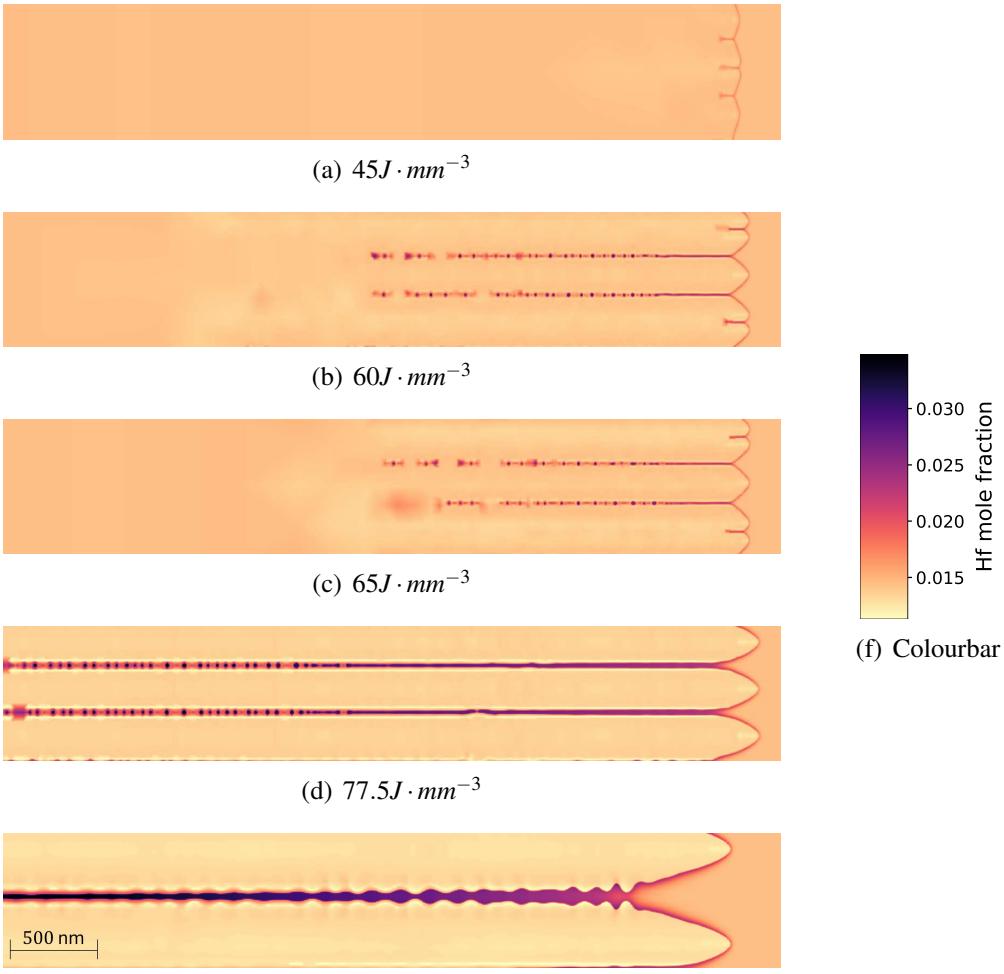

(a) $45J \cdot mm^{-3}$

(b) $60J \cdot mm^{-3}$

(c) $65J \cdot mm^{-3}$

(d) $77.5J \cdot mm^{-3}$

(e) $142.5J \cdot mm^{-3}$

(f) Colourbar

Figure 11: Heatmaps showing the composition of hafnium near the tip of the solidifying microstructure. Increasing the energy density changes the morphology from planar-cellular in (a) to finally dendritic in (e). The microsegregation increases with increasing energy density. Only hafnium is shown in these heatmaps, but the same trend of increasing segregation was seen for all the other alloying components.

$$S^i_{\%} = \left[\frac{c^i}{c^i_{\text{nom}}} - 1\right] \times 100 \tag{25}$$

Table 6: The maximum percentage segregation with respect to the nominal composition, and the corresponding weight percent of segregated elements in the enriched regions. The data in this table is obtained from the phase-field model at 50 K below the solidus to account for non-equilibrium solidification.

Energy Density ($J \cdot mm^{-3}$)	% Segregation				wt.% in Enriched Region			
	Hf	Ta	Ti	W	Hf	Ta	Ti	W
45	+2.8	+1.0	+0.5	-0.5	1.36	3.06	0.67	8.95
60	+63.7	+17.0	+7.1	-1.5	2.14	3.50	0.70	8.75
65	+36.2	+15.2	+5.1	-0.5	1.79	3.46	0.69	8.87
77.5	+525.7	+129.4	+54.1	-68.7	7.89	6.61	0.97	2.68
142.5	+502.3	+129.4	+53.0	-68.7	6.20	6.09	0.91	4.29

Moreover, SEM BSE images were taken of the samples in the build direction (BD), and are shown in Figure 12. The SEM images demonstrate an increase in PDAS with increasing energy density. It also shows a transition from a highly cellular microstructure at 45 $J \cdot mm^{-3}$ to a columnar-dendritic morphology at 142.5 $J \cdot mm^{-3}$. Notice also that the region captured in Figure 12(a) does not show any significant microsegregation at the cell boundaries, while Figure 12(e) clearly shows microsegregation in the interdendritic region.

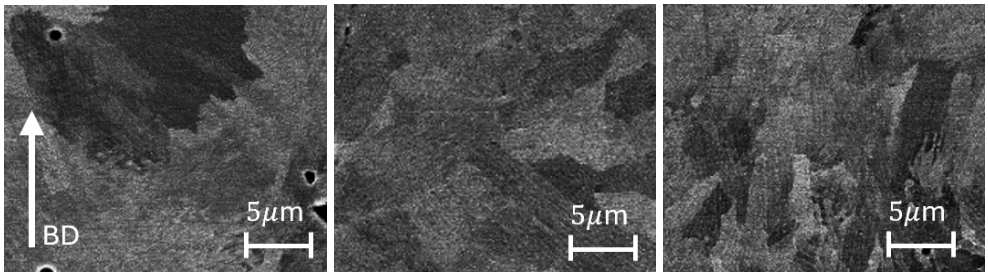

(a) 45 $J \cdot mm^{-3}$ (b) 60 $J \cdot mm^{-3}$ (c) 65 $J \cdot mm^{-3}$

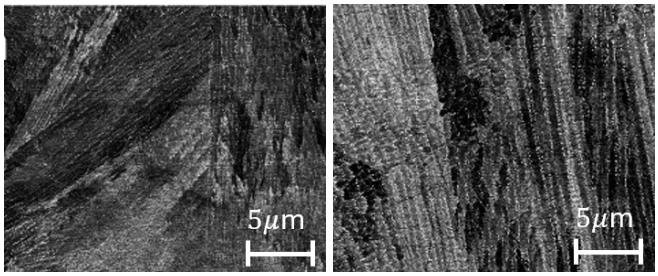

(d) 77.5 $J \cdot mm^{-3}$ (e) 142.5 $J \cdot mm^{-3}$

Figure 12: BSE SEM images of the five energy densities investigated in this study. The build direction (BD) is shown in (a).

4.2. Thermal Gradient and Cooling Rate

Although the thermal gradient and cooling rate are physically coupled in laser powder bed fusion, they were varied independently here to isolate their individual effects on nanovoid formation and solidification morphology. In practice, both parameters vary simultaneously with processing conditions, making it difficult to identify which variable primarily governs pore size and microsegregation. Decoupling them in a controlled numerical framework allows their first-order influences to be assessed independently.

This approach also enables mapping of solidification morphology transitions across $\frac{dT}{dy}$ – R space and identification of parameter regimes associated with reduced nanovoid size and improved interface stability. Such a mapping provides a physical basis for identifying regions of the processing window that may improve printability.

Finally, since both thermal gradient and cooling rate fluctuate near the fusion boundary, varying them independently allows the sensitivity of nanovoid formation to local solidification conditions to be quantified. To manage computational cost, the reduced test matrix in Figure 13(a) was used to capture first-order trends.

4.2.1. Size Distributions

The effect of the thermal gradient and the cooling rate are shown in Figures 13(b)-(c) and 13(d)-(e), respectively. It can be seen that increasing either the thermal gradient or the cooling rate (independently) reduces the mean nanovoid radius. Moreover, the distribution of pores is observed to move from being bimodal to unimodal at more severe thermal gradients. The dendritic structures shown in Figure 14 qualitatively confirm this transition from bimodality to unimodality. This is also evident from the probability density curves in Figure 13(c), which show a double-peaked curve changing into curves with a single maximum.

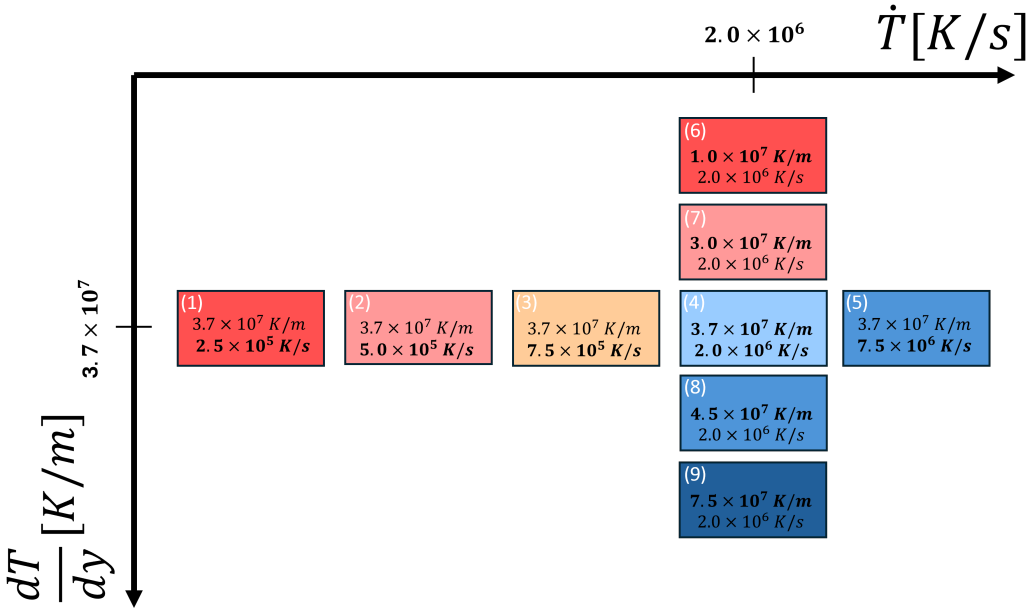

(a) Simulation Test Matrix

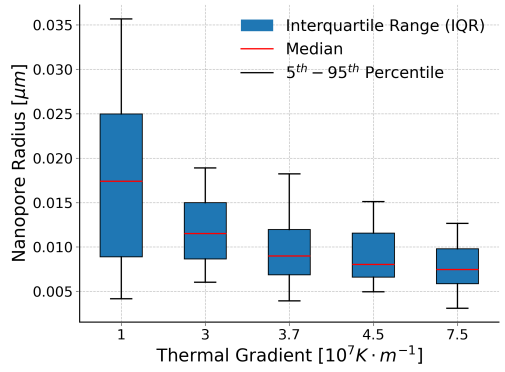

(b)

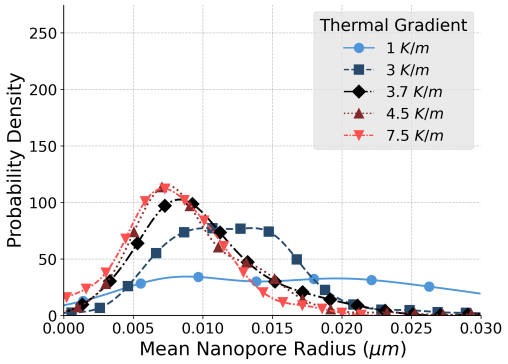

(c)

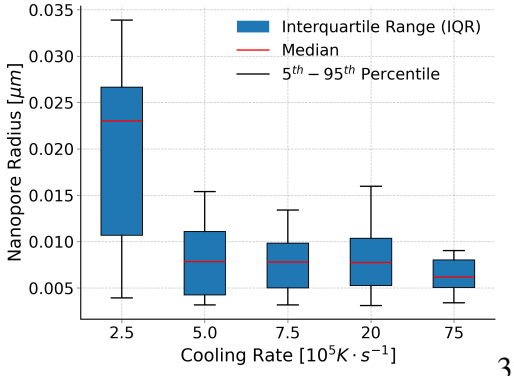

(d)

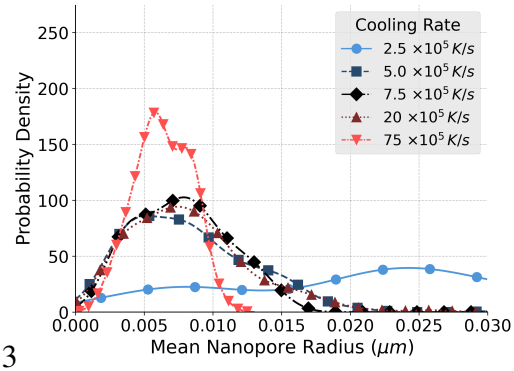

(e)

Figure 13: Effect of varying the thermal gradient on the nanovoid radius distribution.

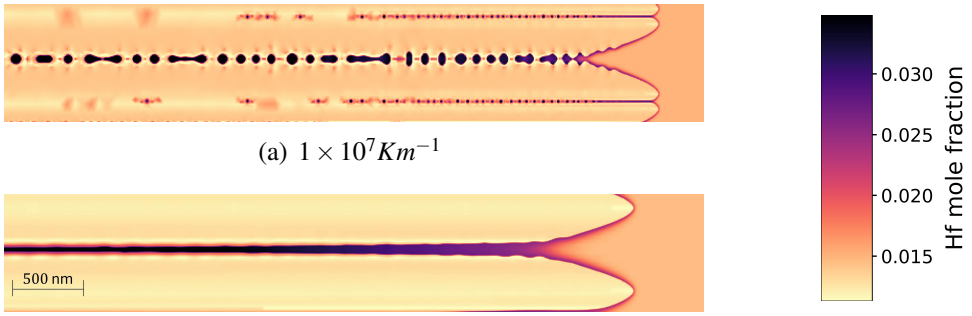

(a) $1 \times 10^7 Km^{-1}$

(b) $3.7 \times 10^7 Km^{-1}$

(c) Colorbar

Figure 14: The change in the distribution of nanovoids from being bimodal in (a) to becoming unimodal under the application of a more severe thermal gradient in (b). Only approximately 5 μm of the domain is shown in Figures (a) and (b).

Although the cooling rate also reduced the mean nanovoid radius and range, the dendrites did not transform into doublons at low cooling rates. The effect of the cooling rate on the distribution of the nanovoids is shown in Figures 13(d) and 13(e). Similarly to the thermal gradient case, the lowest cooling rate produced a bimodal distribution. As opposed to the thermal gradient case, however, the bimodality was caused by a change in the PDAS with build height, which resulted in a changing distribution of pores. A similar effect was observed in some of the simulations by Lindroos et al. [13] who conducted directional solidification simulations at similarly large thermal gradients and cooling rates.

Further insight can be obtained by plotting the solidification morphology on a Growth Rate - Thermal Gradient (GR) plot. This can be shown in Figure 15. The numbers in Figure 15(a) correspond to the numbered bubbles in Figure 15(b). The simulations that produced the largest nanovoids were the lowest thermal gradient case (6) and the lowest cooling rate case (1). This can be explained in the context of the GR plot by the large inter-cellular channel in (1), which leads to larger pores being created and (6) where the structure is strongly dendritic and therefore traps a large number of pores between its secondary dendrite arms. On the other hand, the simulations that produced the smallest - and fewest - nanovoids were the

high cooling rate case (5) and the high thermal gradient one (9). The high cooling rate produced many cells with very small inter-cellular channels that lead to small nanovoids. With the high thermal gradient case, the inter-cellular channels were very small and disappeared quickly with the distance from the tip of the cells. If the thermal gradient is increased further, a planar solidification morphology would be expected. This is an important result because it demonstrates that to minimise the trapping of nanovoids that either a large thermal gradient or a high cooling rate should be targeted. The former risks forming keyhole porosity and the latter lack-of-fusion porosity.

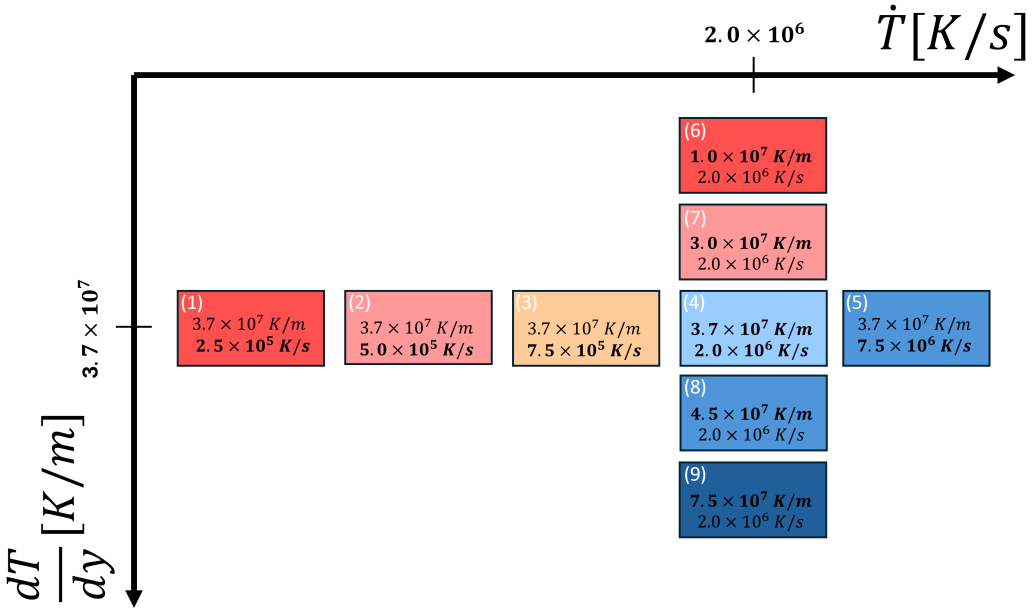

(a) Simulation Test Matrix

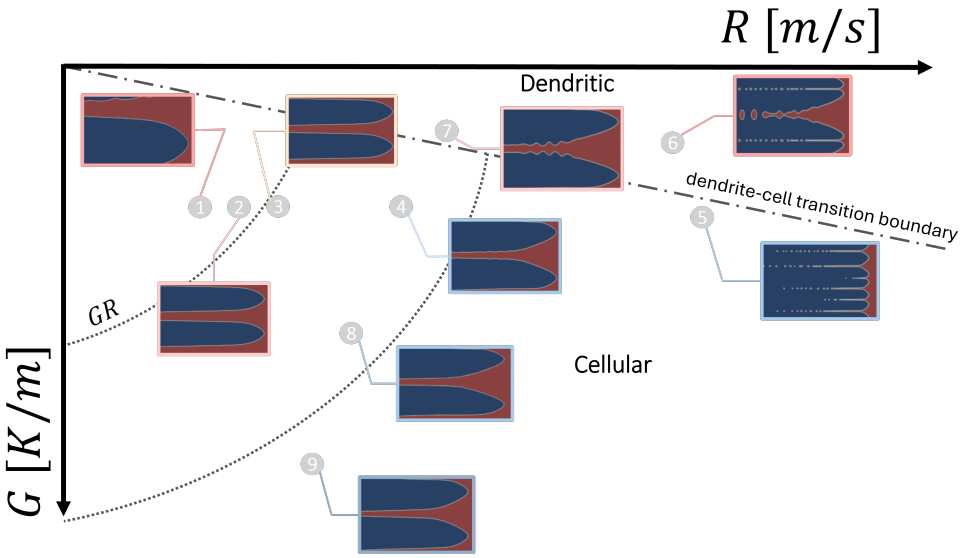

(b) Simulated Morphologies on GR Plot

Figure 15: The effect of the $\frac{dT}{dy} - R$ position on the morphology of the solidification structures.

4.2.2. Concentration Profiles

The thermal gradient did not have any effect on the degree of microsegregation within the thermal gradient range that was investigated. This applies to the concentration at all sampling temperatures. As a result, the concentration profiles for the thermal gradient study are not displayed in this section. The cooling rate, however, caused substantial reduction in microsegregation as the cooling rate was increased from $2 \times 10^6 K \cdot s^{-1}$ to $7.5 \times 10^6 K \cdot s^{-1}$. This change in percentage segregation is reflected in Figure 16. The increase in the number of peaks in Figure 16(b) compared with 16(a) is due to a marked decrease in the PDAS between these two simulations. In Figure 16, ΔT refers to the temperature below the solidus isotherm.

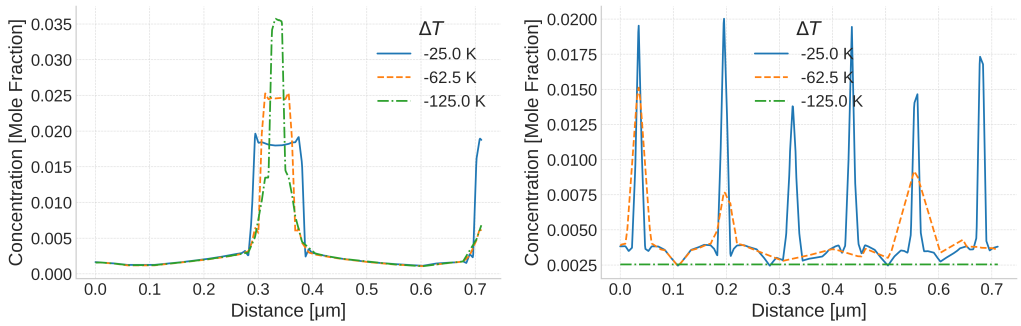

(a) $2.0 \times 10^6 K \cdot s^{-1}$ (b) $7.5 \times 10^6 K \cdot s^{-1}$

Figure 16: The change in the concentration profile of Hf in increasing the cooling rate from $2.0 \times 10^6 K \cdot s^{-1}$ to $7.5 \times 10^6 K \cdot s^{-1}$.

4.3. Growth Angles

The columnar solidification simulations presented until this point have featured perfectly vertical dendritic growth. This is justified because the solidification microstructure in SLM has a strong columnar texture in the $< 100 >$ direction. However, to account for columnar growth at an angle to the $< 100 >$ direction, solidification simulations were performed with reference growth angles ranging from 45 ° to 90 °. A thermal gradient and cooling rate of $2.5 \times 10^7 K \cdot m^{-1}$ and 2

$\times 10^6 K \cdot s^{-1}$ were respectively applied to all the simulations in this section. Physically, the meaning of the reference growth angle is illustrated in Figure 6(b). A total of seven reference growth angles were simulated in this section. The purpose of conducting this study was to understand whether the orientation of the growing dendrites has an effect on the distribution of nanovoids and microsegregation. Practically, this is important since it informs AM practitioners on the influence of columnar grain tilt on the quality of the fabricated parts.

4.3.1. Size Distributions

The qualitative effect of changing the reference growth angle on the pore distribution is shown in Figure 17. Only four of the seven reference angle simulations are shown for clarity. Figure 17 illustrates how the reference growth angle θ_0 was reflected in the simulation. More specifically, the dendrites' orientation was controlled by changing the θ_0 parameter in the interfacial energy term shown in Equation 4. Notice that the thermal gradient is the same for all seven cases in this study, where the thermal gradient is parallel to the long edge of the simulation domain.

(a) 45°

(b) 50°

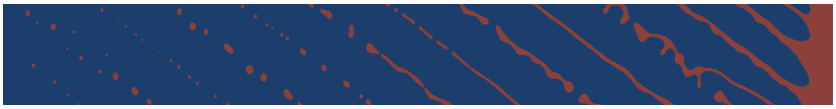

(c) 55°

(d) 60°

(e) 65°

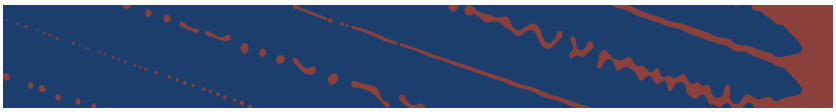

(f) 70°

(g) 90°

Figure 17: The solidification pattern for different growth angles, which represents growth in a direction about the vertical. Notice that only the regions near the tip are shown in this figure for clarity.

The effect of the growth angles on the nanovoid radius and standard deviation is

shown in Figure 18. By consulting the figure, it is clear that increasing the growth angle increased the mean radius of the nanovoids as well as the standard deviation of the pore radius. More acicular pores were observed with increasing growth angles, although the change in the mean aspect ratio was quite small. This can be qualitatively noted from the solidifying simulation domains in Figure 17, which shows more elongated interdendritic liquid pockets in the 90° case than any of the smaller reference growth angles.

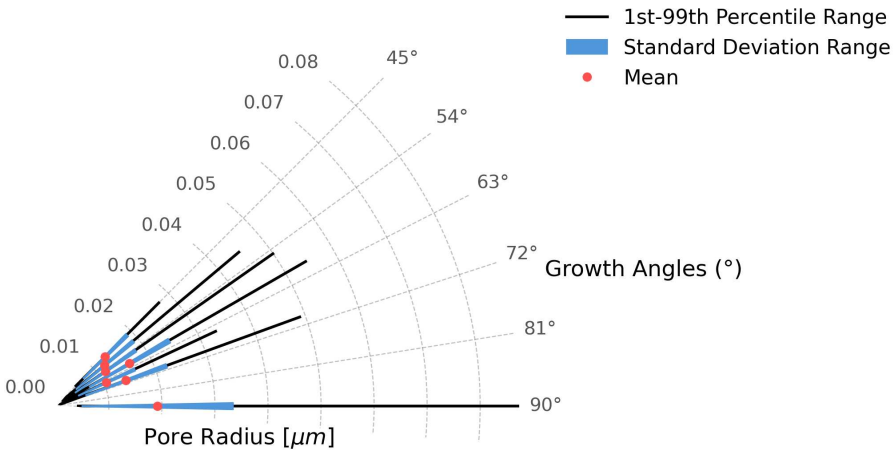

(a)

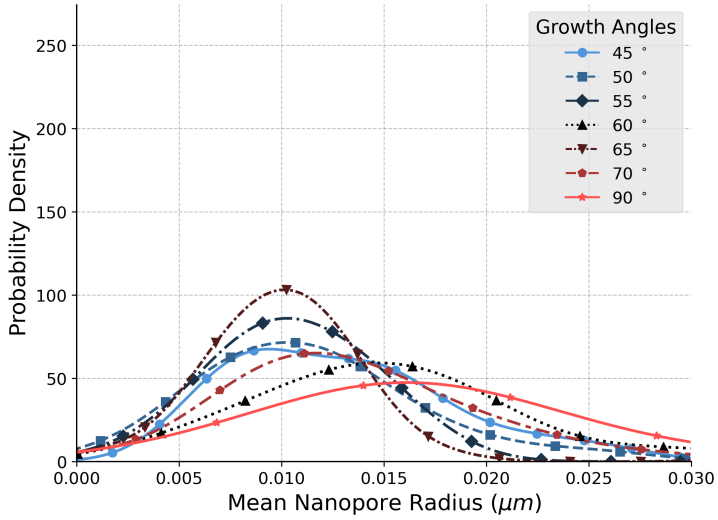

(b)

Figure 18: The effective probability density curves for the growth angles in this paper.

4.3.2. Concentration Profile

The concentration of Hf is reported in Figure 19 for the 45° and 90° growth angles, respectively. The compositional range is the same for both cases, which indicates that the orientation of the growing dendrite does not impact elemental segregation.

For brevity, only the composition of hafnium is shown in Figure 19, but the effect on elemental segregation of the other constituents is the same.

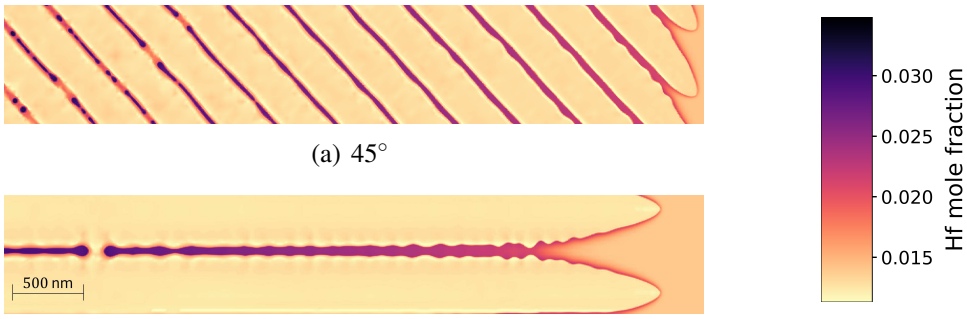

(a) 45°

(b) 90°

(c) Colorbar

Figure 19: The effect of the growth angle on the Hf concentration profile. Notice that Figures (a) and (b) only show approximately 5 μm of the full domain's length for clarity.

5. Discussion

5.1. Microcracking Mechanism

This work aimed to relate SLM processing conditions to the resulting solidification microstructure and, thereby, explain the observed dependence of microcracking on energy density. The authors propose that microcrack formation in SLM is initiated with the development of stable rows of nanovoids, as illustrated in Figure 20(a). These nanovoids subsequently coalesce to form a microcrack at the boundaries between cells or dendrites, as shown in Figure 20(b). Consistent with this mechanism, larger acicular pores are expected to be more prone to forming elongated microcracks than smaller, more equiaxed pores. Although the present study does not explicitly model void growth or coalescence, this proposed mechanism provides a plausible link between nanovoid size and morphology and the propensity for microcrack formation. Further support for this mechanism is provided by Templeton et al. [15], who demonstrated that shrinkage pores can coalesce to form elongated cracks in interdendritic regions of In718.

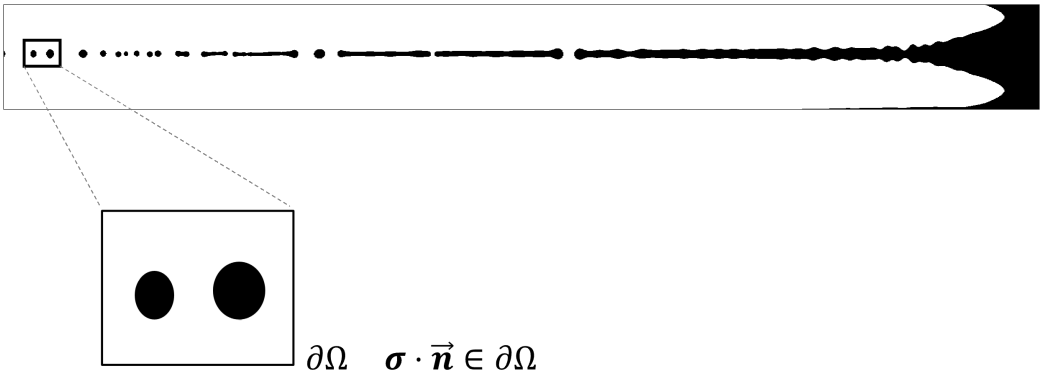

(a)

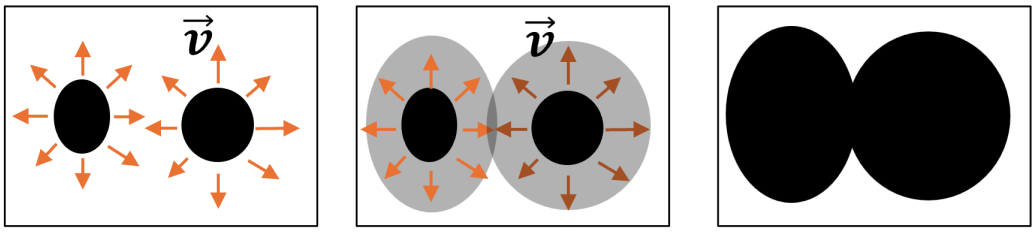

(b)

Figure 20: The formation of a stable row of nanovoids is shown in (a) and its coalescence during loading is illustrated in (b). The orange arrows indicate the velocity of the pores' surfaces as the pores expand.

The present phase-field model does not explicitly resolve the physics of void nucleation and therefore does not simulate pore formation directly. Instead, shrinkage porosity is inferred geometrically by identifying isolated liquid regions at late stages of solidification, which are assumed to transform into pores as a result of insufficient interdendritic feeding during solidification shrinkage. As a result, the predicted pore statistics represent relative trends in porosity formation rather than absolute nucleation behavior and should be interpreted as a comparative measure of printability rather than a direct prediction of experimentally observed pore populations. This assumption is justified by the large solidification shrinkage of liquid nickel ($\rho_s/\rho_l \approx 1.15$), which strongly promotes pore formation in isolated liquid domains. Moreover, the trend of increasing nanovoid radius with energy density

and the concurrent increase in microcracking in Section 4.1 indicates that microcracks are initiated at nanovoids and that they grow through coalescence. Further evidence of this is provided by Fardan et al. [45] who showed that the microcracked surfaces often have dendrites present on either side, which provides direct support for this mechanistic view.

Importantly, even if liquid feeding is sufficient to prevent the formation of shrinkage pores, these entrapped liquid pockets serve as sites for the precipitation of secondary phases, such as MC carbides. The presence of nano-scaled, Hf/Ta-rich MC carbides is well-documented in SLM-processed CM247LC [11, 33]. Some authors, such as Carter et al. [46], suggest that such carbides are responsible for microcracking via solid-state mechanisms like Ductility Dip Cracking (DDC). Regardless of whether failure initiates through late-stage solidification shrinkage or a solid-state mechanism like DDC, we postulate that the isolated liquid pockets predicted by the phase-field model serve as the fundamental precursor for the formation of these deleterious features.

In regions where shrinkage does not lead to nanovoid formation, the interdendritic zones still experience significant residual stresses and localized deformation during the rapid cooling cycles characteristic of SLM. This results in the high dislocation densities observed at cell boundaries in TEM studies by Divya et al. [33] and Wang et al. [47]. This localized accumulation of dislocations, effectively forming internal sub-grain orientations or low-angle boundaries, likely alters the plastic response of the material. The width of the simulation in this work is less than 2 μm, while the results by Divya et al. [33] showed that variations in intra-granular orientations are very small over a two-micron length scale. Hence, orientation changes of the dendrites and cells were not considered in this work.

5.2. Energy Density

Simulations were performed to establish if the nanovoid distribution could be correlated with microcracking in the manufactured samples. The average nanovoid radius ranged from 7 nm to 15 nm when energy densities of $60J \cdot mm^{-3}$ and

$142.5 J \cdot mm^{-3}$ were applied, respectively. The mean nanovoid radius was found to increase with increasing energy density, which corresponds with the positive correlation between energy density and the prevalence of microcracks in the manufactured samples. This can be explained by the decrease in interface stability with increasing energy density, which can be seen by the change of solidification morphology from planar-cellular at 45 $J \cdot mm^{-3}$ to cellular at 60 $J \cdot mm^{-3}$ to dendritic at 142.5 $J \cdot mm^{-3}$. These results are consistent with the findings of Templeton et al. [15] who demonstrated that decreasing the cooling rate produced shrinkage porosity in the interdendritic region. Importantly, in both the manufactured samples and the solidification simulations, there is an evident transition from cellular morphology at low energy density to dendritic morphology at the highest energy density, which is clearly visible from the SEM images in Figure 12. This argument is well-aligned with the mechanistic explanation provided by Templeton et al. [15], who experimentally correlated the SDAS with the propensity for cracking. Evidently, a smaller SDAS is related to a more dendritic morphology. Therefore, the multi-component phase-field model in this paper demonstrated that the change from cellular to dendritic structures can be reasonably predicted using the derived thermal history from FEM conduction model.

Further, the simulation results in Figure 7(b) together with the predictions of nanoporosity in Figure 7(a) indicate that the mean nanovoid radius provides a useful measure for the printability of CM247LC. This statement is supported by the Crystal Plasticity (CP) simulations presented by Lindroos et al. who showed that greater stress concentrations are observed for rapid solidification processes around larger nanoscale pores [13]. It therefore stands to reason that the size distribution of these pores, which are inevitably linked to the dendritic/cellular morphology has a direct effect on the printability of the alloy. A more comprehensive analysis of printability requires microresidual stresses to be predicted in tandem with the phase-field simulations. Nonetheless, it can be said phenomenologically that increasing microsegregation together with an increase in nanovoid radius would lead to greater cracking propensity due to an increased mismatch in

thermal expansivity and the existence of larger crack-initiation sites.

The degree of elemental segregation was captured by the phase-field model and reported in Table 6. Minimal segregation was observed in the lowest energy density case, primarily because the morphology developed into a fast-moving flat interface that trapped the majority of the solute in the solid. The percentage segregation increased with increasing energy density, since the morphology steadily transitioned to become more dendritic and therefore produced more intercellular/interdendritic channels that solute could diffuse to. There was no marked difference in percentage segregation for the final two cases. This provides a further explanation for the beginning of microcracking at 77.5 $J \cdot mm^{-3}$, since the difference in composition between the dendrites and the final liquid increases the mismatch in thermal expansivity and therefore produces greater microresidual stresses on cooling. Although quantitative experimental measurements of segregation were not included in this study, the BSE SEM images in Figure 12 demonstrate, qualitatively, that solute segregation increases with energy density. The composition of hafnium at a grain boundary was reported by Fardan et al. [44] for CM247 using Atom Probe Tomography (APT) to be 6 wt. % for an energy density of 75 $J \cdot mm^{-3}$. The wt. % composition in the segregated regions was calculated from the phase-field simulations to be 7 wt. % at 77.5 $J \cdot mm^{-3}$ and retained a similar value of 6 wt. % at 142.5 $J \cdot mm^{-3}$. This indicates that the phase-field simulations provide a compositionally accurate picture. Further, the SEM images in Figure 12 also corroborate the phase-field simulation results in Figure 11, since they both demonstrate an increase in PDAS with energy density.

Finally, the experimental and numerical results from the energy density investigation explain why CM247LC and other high-γ' alloys are so difficult to print. That is, in order to print CM247LC without microcracking the cooling rate needs to be sufficiently high to suppress dendrite formation. With a standard (Gaussian) beam shape, and traditional optimisation, this would lead to lack-of-fusion porosity. A similar observation was made by Fardan et al. [45] but was not mechanistically explained. This leads to the conclusion that in order to print CM247LC

in a porosity-free, crack-free condition the thermal history needs to be controlled to achieve a high-enough cooling rate while ensuring full melting of the metal powder to avoid lack-of-fusion porosity.

5.3. Thermal Gradient and Cooling Rate

Increasing either the thermal gradient or the cooling rate decreased the mean nanovoid radius. These results are in alignment with the experimental observations made by Templeton et al. [15]. While increasing the cooling rate eventually resulted in a marked reduction of percentage segregation, the thermal gradient did not have a discernible effect on the degree of elemental segregation. The reduction in microsegregation as well as the reduction in nanovoid size invariably improve the print quality. An interesting observation in the thermal gradient study is the formation of a bimodal nanovoid distribution at the lowest thermal gradient, which is directly caused by the formation of a doublon structure at the dendrites' tips. The formation of doublons has been observed experimentally in metallic as well as non-metallic compounds [21, 48]. Doublon formation is associated with stronger microsegregation and lower interface stability [48]. However, to the author's knowledge, doublons - or other tip-branching effects - have not been reported in the Additive Manufacturing (AM) literature previously. The importance of the pore distribution's bi-modality is therefore unknown. It is likely that the distribution with the greater nanovoid radii (those associated with the inter-dendritic region) would be responsible for the cracking behaviour. Alternatively, the proximity of the two pore distributions may initiate an interaction that expedites crack formation. Micro-residual stress simulations are needed to ascertain the influence of multi-modal pore distributions on pore formation. Nevertheless, the mean nanovoid diameter is considerably larger for the lowest thermal gradient case, which will have an adverse effect on the printability of the alloy irrespective of the distribution type.

The results in Figure 15 showed that to reduce the size of trapped nanovoids, either the thermal gradient or the cooling rate should be increased. This is because in-

creasing the thermal gradient brings the solidification morphology closer to being planar rather than cellular and reduces the width of the inter-cellular region, which is where the trapping would occur. On the other hand, increasing the cooling rate produces many more cells with smaller inter-cellular regions between them. This also has the effect of decreasing the size of the trapped nanovoids. Heuristically, it is known that to get a stronger thermal gradient that a greater energy density is needed, which was generally seen in Section 4.1; while getting a higher cooling rate requires a lower energy density [49]. Therefore, to obtain a thermal gradient that is large enough to suppress the formation of nanovoids there is a risk of keyholing. Similarly, to obtain a high enough cooling rate to prevent nanovoid trapping, the laser would risk entering the lack-of-fusion zone. To better illustrate this, Figure 21 is used to demonstrate where in the processing window cellular and planar microstructures would be expected, and how that correlates with keyholing and lack-of-fusion porosity. Figure 21(a) represents a difficult-to-print alloy such as CM247LC where a large cooling rate is needed to produce a highly cellular morphology. Figure 21(b) on the other hand shows an alloy that is more printable where there is an overlap between the region of cellular morphology and the 'Dense' region. It is important to note that Figure 21 is only meant to be illustrative for the purpose of establishing trends and relationships rather than to provide an accurate quantitative picture.

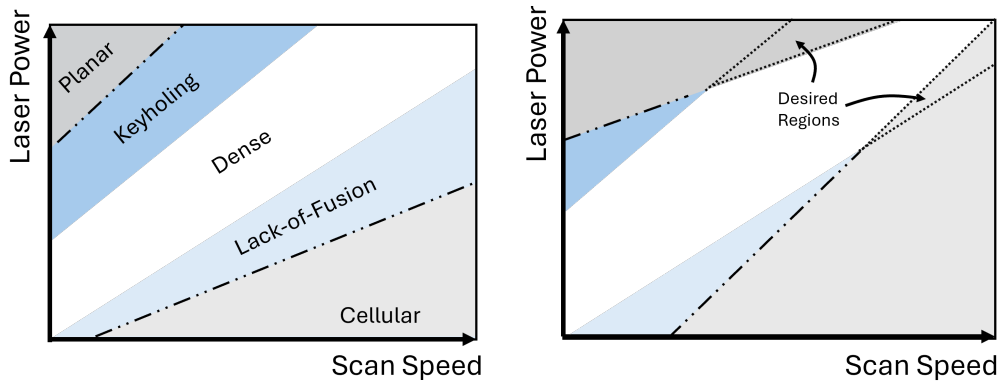

(a) Microcracking (b) No Microcracking

Figure 21: Schematic illustration of the qualitative relationship between SLM processing conditions, defect formation (lack of fusion and keyholing), and solidification morphology (cellular, dendritic, and planar). Panel (a) represents a difficult-to-print alloy, while the alloy in (b) is more printable.

Based on the aforementioned arguments, it is clear that the difficulty in printing CM247LC is that suppressing the trapping of nanovoids in the inter-cellular or interdendritic regions encroaches on the processing zones that cause lack-of-fusion or keyhole porosity. This conclusion is supported by the work of Hu et al. [36], where removing hafnium was shown to reduce crack sensitivity in CM247. According to the Mullins-Sekerka stability criterion in Equation 26, increasing the partition coefficient k increases the stability of the interface, which is what happens when the freezing range is reduced [40]. In Equation 26, Γ is the Gibbs-Thomson coefficient, and v is the steady-state interface velocity. This means that the removal of Hf produced an alloy with a more stable solidification front that is less likely to form dendrites even at lower cooling rates, which provides a larger processing window.

$$A = \frac{k^2 \Gamma v}{m C_0 (1-k) D_L}, \tag{26}$$

In conclusion, the pattern of nanovoid distributions given in Section 4.2 supports the theory that the microcracking of CM247LC and other similar alloys is mediated by the formation and growth of nanovoids. It also provides an explanation as to why CM247LC remains difficult to print in the face of the many experimental studies dedicated to it in the literature [36, 50, 51, 52, 53, 45].

5.4. Growth Angles

Although the dendrites predominantly grow parallel to the build direction, columnar grains are often reported to tilt with respect to the build direction. It is clear from the simulation results in Figures 17 and 18 that the growth angle has a measurable impact on the final distribution of nanovoids. Growing exactly parallel to the build direction produces the largest mean nanovoid radius and the greatest standard deviation range of pore radius. Although the larger mean radius could indicate that a growth angle of 90° is the most likely to fail, this must be considered contextually since changing scanning strategies can result in complex microstructural and thermal changes [8].

Tilt of columnar grains is rarely referred to in the experimental literature on SLM since tilt typically varies as a result of controlling the texture [8, 54]. Nonetheless, it is clear from the work of Thijs et al. [54] that processing parameters can have a strong influence on the direction of epitaxial growth during solidification. For CM247LC, the work by Carter et al. [46] showed that changing the scanning strategy produced a bimodal microstructure where the columnar grains grew at an angle to the building direction [8]. Since increasing the dendrites' growth angle was shown to increase the mean nanovoid radius, it is reasonable to suggest that processing conditions should favour tilting the columnar grains to improve printability. This, however, must be balanced with the other factors mentioned in this work, including the energy density, thermal gradient, and cooling rate.

Changing the growth angles did not affect the concentration profile of the solidified domain, meaning that the influence of the growth angle is through the distribution of nanovoids that it produces, as well as the alignment of the bound-

ary tractions with the dendrites' primary axes. The latter influence can only be revealed using a multi-scale approach that begins with calculating tractions on the grain boundaries.

6. Conclusions

This work investigated how location-specific thermal history and grain growth orientation at the fusion boundary govern solidification morphology and nanovoid formation in CM247LC during SLM. By combining conduction-based thermal modelling with a multicomponent phase-field framework, the effects of energy density, thermal gradient, and cooling rate on local solidification behaviour were quantified and linked directly to experimentally observed microcracking.

- The nanovoid populations predicted by the phase-field model establish a mechanistic, location-specific link between solidification morphology and microcrack susceptibility in CM247LC. Cellular growth reduces the width of intercellular channels near the solidification front, suppressing the formation of shrinkage-induced nanovoids relative to dendritic growth.
- The processing window required to maintain a fully cellular solidification morphology—and therefore minimise nanovoid formation—demands sufficiently high local cooling rates. However, increasing cooling rate simultaneously drives the process into the lack-of-fusion regime. Conversely, increasing energy density suppresses lack-of-fusion porosity but promotes dendritic growth and nanovoid formation. This morphology-driven trade-off, governed by interface stability rather than process parameters alone, restricts crack-free SLM of CM247LC using conventional Gaussian beams.
- The experimentally observed increase in microcrack density as the morphology becomes more dendritic, together with the predicted growth and clustering of nanovoids, supports a solidification-driven cracking mechanism in which nanovoids form within interdendritic regions due to solidification shrinkage and subsequently coalesce to form microcracks during

cooling or loading.

- The largest nanovoids are observed when dendritic growth is parallel to the thermal gradient; increasing the growth angle reduces nanovoid size and variability. This suggests that maintaining a slight misalignment between grain growth direction and the thermal gradient may be beneficial for suppressing interdendritic void formation.

To the authors' knowledge, this work represents the first physics-based, multicomponent phase-field study to resolve location-specific solidification morphology and nanoscale porosity formation in a high-γ' Ni-based superalloy under SLM conditions, and to directly link these phenomena to microcracking. These findings demonstrate that the cellular–dendritic transition constrains the crack-free processing window of high-γ' Ni-based superalloys. Achieving crack-free fabrication will therefore require thermal histories that promote sustained cellular growth while ensuring full fusion, or alternative beam shaping and alloy design strategies that enhance solidification interface stability.

7. Acknowledgements

This work was completed as part of the Eng.D. programme at the University of Sheffield within the Advanced Metallic Systems Centre for Doctoral Training (CDT). The Eng.D. is supported by the EPSRC under Grant EP/S022635 and receives industrial support from GKN Aerospace, including access to facilities at the Global Technology Centre. The authors also thank Dr. George Maddison for facilitating the production of experimental samples at the Royce Discovery Centre, University of Sheffield.

References

[1] Amir Mostafaei, Reza Ghiaasiaan, I-Ting Ho, Seth Strayer, Kai-Chun Chang, Nima Shamsaei, Shuai Shao, Santanu Paul, An-Chou Yeh, Sammy

Tin, et al. Additive manufacturing of nickel-based superalloys: A state-of-the-art review on process-structure-defect-property relationship. *Progress in Materials Science*, 136:101108, 2023.

[2] D. Marini et al. Near net shape manufacturing: A review of approaches and their evolutions. *Proceedings of the Institution of Mechanical Engineers, Part B: Journal of Engineering Manufacture*, 232(4):652–667, 2018.

[3] M. Sun et al. Additive manufacturing of nickel-based superalloys: opportunities and challenges. *Materials Today Advances*, 10:100078, 2020.

[4] Chor Yen Yap, Chee Kai Chua, Zhi Li Dong, Zhong Hong Liu, Dan Qing Zhang, Loong Ee Loh, and Swee Leong Sing. Review of selective laser melting: Materials and applications. *Applied physics reviews*, 2(4), 2015.

[5] Salomé Sanchez, Peter Smith, Zhengkai Xu, Gabriele Gaspard, Christopher J. Hyde, Wessel W. Wits, Ian A. Ashcroft, Hao Chen, and Adam T. Clare. Powder bed fusion of nickel-based superalloys: A review. *International Journal of Machine Tools and Manufacture*, 165:103729, 2021.

[6] Moataz M Attallah, Rachel Jennings, Xiqian Wang, and Luke N Carter. Additive manufacturing of ni-based superalloys: The outstanding issues. *MRS bulletin*, 41(10):758–764, 2016.

[7] Apratim Chakraborty, Waqas Muhammad, Jean-Philippe Masse, Reza Tangestani, Morteza Ghasri-Khouzani, Andrew Wessman, and Étienne Martin. Role of alloy composition on micro-cracking mechanisms in additively manufactured ni-based superalloys. *Acta Materialia*, 255:119089, 2023.

[8] Luke N Carter, Christopher Martin, Philip J Withers, and Moataz M Attallah. The influence of the laser scan strategy on grain structure and cracking behaviour in slm powder-bed fabricated nickel superalloy. *Journal of Alloys and Compounds*, 615:338–347, 2014.

[9] Edouard Chauvet, Paraskevas Kontis, Eric A Jägle, Baptiste Gault, Dierk Raabe, Catherine Tassin, Jean-Jacques Blandin, Rémy Dendievel, Benjamin Vayre, Stéphane Abed, et al. Hot cracking mechanism affecting a non-weldable ni-based superalloy produced by selective electron beam melting. *Acta Materialia*, 142:82–94, 2018.

[10] Bey Vrancken, Ruben Wauthlé, Jean-Pierre Kruth, and Jan Van Humbeeck. Study of the influence of material properties on residual stress in selective laser melting. In *Proceedings of the solid freeform fabrication symposium*, pages 393–407, 2013.

[11] Yuanbo T Tang, Chinnapat Panwisawas, Joseph N Ghoussoub, Yilun Gong, John WG Clark, André AN Németh, D Graham McCartney, and Roger C Reed. Alloys-by-design: Application to new superalloys for additive manufacturing. *Acta Materialia*, 202:417–436, 2021.

[12] HC Basoalto, C Panwisawas, Y Sovani, MJ Anderson, RP Turner, B Saunders, and JW Brooks. A computational study on the three-dimensional printability of precipitate-strengthened nickel-based superalloys. *Proceedings of the Royal Society A*, 474(2220):20180295, 2018.

[13] Matti Lindroos, Tatu Pinomaa, Kais Ammar, Anssi Laukkanen, Nikolas Provatas, and Samuel Forest. Dislocation density in cellular rapid solidification using phase field modeling and crystal plasticity. *International Journal of Plasticity*, 148:103139, 2022.

[14] Tatu Pinomaa, Matti Lindroos, Paul Jreidini, Matias Haapalehto, Kais Ammar, Lei Wang, Samuel Forest, Nikolas Provatas, and Anssi Laukkanen. Multiscale analysis of crystalline defect formation in rapid solidification of pure aluminium and aluminium–copper alloys. *Philosophical Transactions of the Royal Society A*, 380(2217):20200319, 2022.

[15] William Frieden Templeton, Shawn Hinnebusch, Seth T. Strayer, Albert C. To, P. Chris Pistorius, and Sneha Prabha Narra. A mechanistic explanation of

shrinkage porosity in laser powder bed fusion additive manufacturing. *Acta Materialia*, 266:119632, 2024.

[16] D. G. Eskin, Suyitno, and L. Katgerman. Mechanical properties in the semi-solid state and hot tearing of aluminium alloys. *Progress in Materials Science*, 49(5):629–711, 2004.

[17] Dongxu Chen, Junsheng Wang, and Chi Zhang. Coupling phase-field model and cfd for hot cracking predictions of al-li alloys. *Computational Materials Science*, 192:110361, 2021.

[18] Lei Wang and Kehong Wang. Investigation on microstructural patterns and hot crack in the molten pool via integrated finite-element and phase-field modeling. *Journal of Manufacturing Processes*, 48:191–198, 2019.

[19] Fei Yang, Jie-shan Hou, Chang-shuai Wang, Lan-zhang Zhou, et al. Effects of solution treatment on microstructure and tensile properties of as-cast alloy 625. *Transactions of Nonferrous Metals Society of China*, 31(2):426–437, 2021.

[20] Larry K Aagesen, Yipeng Gao, Daniel Schwen, and Karim Ahmed. Grand-potential-based phase-field model for multiple phases, grains, and chemical components. *Physical Review E*, 98(2):023309, 2018.

[21] Abhik Choudhury and Britta Nestler. Grand-potential formulation for multicomponent phase transformations combined with thin-interface asymptotics of the double-obstacle potential. *Phys. Rev. E*, 85:021602, Feb 2012.

[22] A. A. Wheeler, W. J. Boettinger, and G. B. McFadden. Phase-field model for isothermal phase transitions in binary alloys. *Phys. Rev. A*, 45:7424–7439, May 1992.

[23] Seong Gyoon Kim, Won Tae Kim, and Toshio Suzuki. Interfacial compositions of solid and liquid in a phase-field model with finite interface thickness

for isothermal solidification in binary alloys. *Phys. Rev. E*, 58:3316–3323, Sep 1998.

[24] Ryo Kobayashi. A numerical approach to three-dimensional dendritic solidification. *Experimental Mathematics*, 3(1):59–81, 1994.

[25] Sudipta Biswas, Dehao Liu, Larry Aagesen, and Wen Jiang. Solidification and grain formation in alloys: A 2d application of the grand-potential-based phase-field approach. *Modelling and Simulation in Materials Science and Engineering*, 30, 12 2021.

[26] Alain Karma. Phase-field formulation for quantitative modeling of alloy solidification. *Physical review letters*, 87(11):115701, 2001.

[27] Folch R. Karma A. Echebarria, B. and M. Plapp. Quantitative phase-field model of alloy solidification. *Physical Review E*, 70:061604, 2004.

[28] Alexander D. Lindsay, Derek R. Gaston, Cody J. Permann, Jason M. Miller, David Andrš, Andrew E. Slaughter, Fande Kong, Joshua Hansel, Robert W. Carlsen, Casey Icenhour, Logan Harbour, Guillaume L. Giudicelli, Roy H. Stogner, Peter German, Jacob Badger, Sudipta Biswas, Leora Chapuis, Christopher Green, Jason Hales, Tianchen Hu, Wen Jiang, Yeon Sang Jung, Christopher Matthews, Yinbin Miao, April Novak, John W. Peterson, Zachary M. Prince, Andrea Rovinelli, Sebastian Schunert, Daniel Schwen, Benjamin W. Spencer, Swetha Veeraraghavan, Antonio Recuero, Dewen Yushu, Yaqi Wang, Andy Wilkins, and Christopher Wong. 2.0 - MOOSE: Enabling massively parallel multiphysics simulation. *SoftwareX*, 20:101202, 2022.

[29] Magnus J. Anderson, Jonathan Benson, Jeffery W. Brooks, Benjamin Saunders, and Hector C. Basoalto. Predicting Precipitation Kinetics During the Annealing of Additive Manufactured Inconel 625 Components. *Integrating Materials and Manufacturing Innovation*, 8(2):154–166, 2019.

[30] Michael Smith. *ABAQUS/Standard User's Manual, Version 6.9*. Dassault Systèmes Simula Corp, 2009.

[31] J-O Andersson, Thomas Helander, Lars Höglund, Pingfang Shi, and Bo Sundman. Thermo-calc dictra, computational tools for materials science. *Calphad*, 26(2):273–312, 2002.

[32] Chunlei Qiu, Haoxiu Chen, Qi Liu, Sheng Yue, and Huaming Wang. On the solidification behaviour and cracking origin of a nickel-based superalloy during selective laser melting. *Materials Characterization*, 148:330–344, 2019.

[33] VD Divya, R Muñoz-Moreno, OMDM Messé, JS Barnard, S Baker, T Illston, and Howard James Stone. Microstructure of selective laser melted cm247lc nickel-based superalloy and its evolution through heat treatment. *Materials Characterization*, 114:62–74, 2016.

[34] Luke Nelson Carter. *Selective laser melting of nickel superalloys for high temperature applications*. PhD thesis, University of Birmingham, 2013.

[35] M.J. Aziz. Model for solute redistribution during rapid solidification. *Journal of Applied Physics*, 53:1158, 1982.

[36] Pengfei Hu, Zhuangzhuang Liu, Miaomiao Chen, Yinghui Li, Xiaohong Qi, and Jianxin Xie. Reducing cracking sensitivity of cm247lc processed via laser powder bed fusion through composition modification. *Journal of Materials Research and Technology*, 29:3074–3088, 2024.

[37] Richard A. Otis and Zi-Kui Liu. High-throughput thermodynamic modeling and uncertainty quantification for icme. *JOM*, 69(5):886–891, 2017.

[38] P. Honarmandi, T. C. Duong, S. F. Ghoreishi, D. Allaire, and R. Arroyave. Bayesian uncertainty quantification and information fusion in calphad-based thermodynamic modeling. *Acta Materialia*, 164:636–647, 2019.

[39] OpenCV team. Opencv library. `https://opencv.org/`, 2000. Accessed: 2025-01-05.

[40] William W Mullins and RF Sekerka. Stability of a planar interface during solidification of a dilute binary alloy. *Journal of applied physics*, 35(2):444–451, 1964.

[41] Neil J. Harrison, Iain Todd, and Kamran Mumtaz. Reduction of micro-cracking in nickel superalloys processed by selective laser melting: A fundamental alloy design approach. *Acta Materialia*, 94:59–68, 2015.

[42] Stanisław Węglarczyk. Kernel density estimation and its application. In *ITM web of conferences*, volume 23, page 00037. EDP Sciences, 2018.

[43] S. Patel and M. Vlasea. Melting modes in laser powder bed fusion. *Materialia*, 9:100591, 2020.

[44] Ahmed Fardan, Andrea Fazi, Jakob Schröder, Tatiana Mishurova, Tobias Deckers, Giovanni Bruno, Mattias Thuvander, Andreas Markström, Håkan Brodin, and Eduard Hryha. Microstructure tailoring for crack mitigation in cm247lc manufactured by powder bed fusion – laser beam. *Additive Manufacturing*, 99:104672, 2025.

[45] Ahmed Fardan, Andrea Fazi, Ru Lin Peng, Tatiana Mishurova, Mattias Thuvander, Giovanni Bruno, Håkan Brodin, and Eduard Hryha. Fine-tuning melt pools and microstructures: Taming cracks in powder bed fusion—laser beam of a non-weldable ni-base superalloy. *Materialia*, 34:102059, 2024.

[46] Luke N Carter, Moataz M Attallah, Roger C Reed, et al. Laser powder bed fabrication of nickel-base superalloys: influence of parameters; characterisation, quantification and mitigation of cracking. *Superalloys*, 2012(6):2826–2834, 2012.

[47] Xiqian Wang, Luke N Carter, Bo Pang, Moataz M Attallah, and Michael H Loretto. Microstructure and yield strength of slm-fabricated cm247lc ni-superalloy. *Acta Materialia*, 128:87–95, 2017.

[48] Wilfried Kurz, Michel Rappaz, and Rohit Trivedi. Progress in modelling solidification microstructures in metals and alloys. part ii: dendrites from 2001 to 2018. *International Materials Reviews*, 66(1):30–76, 2021.

[49] Ankur K. Agrawal, Behzad Rankouhi, and Dan J. Thoma. Predictive process mapping for laser powder bed fusion: A review of existing analytical solutions. *Current Opinion in Solid State and Materials Science*, 26(6):101024, 2022.

[50] S. Markanday, R. J. Moat, H. X. Li, and M. M. Attallah. The microstructural evolution of cm247lc manufactured through laser powder bed fusion. *Metallurgical and Materials Transactions A*, 54:1–15, 2023.

[51] M. Abdelwahed, M. Elbestawi, S. Veldhuis, and M. M. Attallah. Cracking mechanisms and effect of extensive preheating in cm247lc and in713lc ni-base superalloy processed by laser powder bed fusion. *Additive Manufacturing*, 68:103566, 2023.

[52] O. Adegoke, J. Andersson, H. Brodin, and R. Pederson. Influence of laser powder bed fusion process parameters on voids, cracks and microhardness of nickel-based superalloy alloy 247lc. *Materials*, 13(18):4089, 2020.

[53] John H. Boswell, Daniel Clark, Wei Li, and Moataz M. Attallah. Cracking during thermal post-processing of laser powder bed fabricated cm247lc ni-superalloy. *Materials Design*, 174:107793, 2019.

[54] Lore Thijs, Karolien Kempen, Jean-Pierre Kruth, and Jan Van Humbeeck. Fine-structured aluminium products with controllable texture by selective laser melting of pre-alloyed alsi10mg powder. *Acta Materialia*, 61(5):1809–1819, 2013.

[55] Alain Karma and Wouter-Jan Rappel. Quantitative phase-field modeling of dendritic growth in two and three dimensions. *Phys. Rev. E*, 57:4323–4349, Apr 1998.

A. Normalisation

A.1. Allen-Cahn Equation Normalisation

First, we define how the parameters should be scaled for the normalisation. This is done by saying that each parameter is equal to a constant characteristic factor multiplied by the normalised parameter. For time, for example $t = t^* T$, where T is the characteristic time and t^* is the normalised time. Similarly, the height of the multi-well potential, the chemical potential, and the parabola's curvature are written as $m = m_0 m^*$, $\mu = \mu_0 \mu^*$, and $k_b^I = k_b^{I,0} k_b^{I,*}$ respectively.

The characteristic time and length scales (T and ℓ) were calculated from Equations A.1 and A.2 respectively.

$$\tilde{L} = LTm_0 \tag{A.1}$$

$$\tilde{\kappa} = \frac{\kappa}{m_0 \ell^2} \tag{A.2}$$

After assigning the non-dimensional variables, the following condition must be enforced to get a coefficient of unity for the grand-potential function. Ensuring that conditions A.3 and A.4 were satisfied simplified the expressions for the grand potential since coefficients would be reduced to one. This was observed to improve the convergence behaviour of the simulations.

$$\frac{\mu_0^2}{V_m^2 k_{I,0}^{\alpha} m_0} = 1 \tag{A.3}$$

$$\frac{\mu_0}{V_m m_0} = 1 \tag{A.4}$$

A summary of the parameters pertaining to the normalisation of the Allen-Cahn equation is shown in Tables B.8 and B.7. The characteristic time T produced by

this normalisation is 1.79 μs and the characteristic length l_0 is 79.1 nm.

A.2. Cahn-Hilliard Equation Normalisation

Next, the conservation equation for the chemical potential is normalised. By doing this, normalised susceptibility and diffusivity values χ_{II}^0 and D_{II}^0 are determined, respectively. In line with notation in the previous section, $\chi_{II} = \chi_{II}^* \chi_{II}^0$ and $D_{II} = D_{II}^* D_{II}^0$.

$$\frac{\partial \mu_I^*}{\partial t^*} \chi_{II}^* = \tilde{\nabla} \cdot \frac{D_{II^0} D_{II}^* \chi_{II}^* T}{\ell^2} \tilde{\nabla} \mu_I^* - \sum_{\beta=1}^{2} \frac{1}{\chi_{II}^0 \mu_I^0} \frac{\partial \rho_I}{\partial \eta_{\beta 1}} \frac{\partial \eta_{\beta 1}}{\partial t^*} \tag{A.5}$$

Similarly to the Allen-Cahn equation, three conditions will be imposed here. Specifically, Equation A.6 produces the dimensionless diffusivity; Equation A.9 produces the dimensionless susceptibility; and finally, Equations A.9 and A.10 are enforced to ensure that the expression for density has coefficients that are equal to unity.

$$\frac{D_{II^0} T}{\ell^2} = 1 \tag{A.6}$$

The density can be represented as a function of the chemical potential, as shown in Equation A.7.

$$\rho = \frac{\mu_I}{V_m^2 k_I^\alpha} + \frac{c_I^{\alpha,\min}}{V_m} \tag{A.7}$$

This means that the dimensionless density is given by Equation A.8.

$$\rho^* = \frac{\mu_I}{V_m^2 k_I^\alpha \chi_{II}^0 \mu_I^0} + \frac{c_I^{\alpha,\min}}{V_m \chi_{II}^0 \mu_I^0} \tag{A.8}$$

To make sure that the dimensionless expression for density has exactly the same

form as the original equation, we must ensure that the expressions in Equations A.9 and A.10 are equal to unity respectively.

$$\frac{1}{V_m^{0\,2} k_{I,0}^{\alpha} \chi_{II}^{0}} = 1 \tag{A.9}$$

$$\frac{c_{I,0}^{\alpha,\min}}{V_m^0 \chi_{II}^0 \mu_I^0} = 1 \tag{A.10}$$

B. CM247LC Data

B.1. Dimensional

Table B.7: Interface properties of CM247 at a temperature T_0 of 1663K.

Property	Value	Description
V_m $[m^{-3}mol^{-1}]$	1×10^{-5}	Molar Volume
ε $[Jm^{-1}]$	2.3250×10^{-9}	Gradient Energy Coefficient
σ $[Jm^{-2}]$	0.31	Surface Energy
L $[m^3J^{-1}s^{-1}]$	1	Allen-Cahn Mobility
m $[Jm^{-3}]$	1.86×10^8	Double-well Height
T_{solidus} $[K]$	1603	Solidus Temperature
T_{liquidus} $[K]$	1681	Liquidus temperature
T_0 $[K]$	1663	Fusion boundary temperature

Table B.8: Thermodynamic data obtained from ThermoCalc for CM247LC at a temperature T_0 of 1663 K.

Property	Value		Description
	Solid	Liquid	
S $[Jm^{-3}]$	8.92×10^6	9.89×10^6	Entropy Density
C_p $[Jmol^{-1}K^{-1}]$	85.8	159	Specific heat capacity
D_{Hf} $[m^2s^{-1}]$	1.72×10^{-12}	2.87×10^{-9}	
D_{Ta} $[m^2s^{-1}]$	4.89×10^{-14}	2.87×10^{-9}	
D_{Ti} $[m^2s^{-1}]$	1.41×10^{-13}	2.87×10^{-9}	
D_{W} $[m^2s^{-1}]$	5.20×10^{-16}	1.57×10^{-9}	Element tracer self-diffusivities

Table B.9: Parameters of the fitted paraboloid following the translation to match the equilibrium compositions, including additional terms for thermal properties.

	Solid Phase					Liquid Phase				
Element	$\mathbf{k^s_{b,I}}$ (J/m^3)	$\mathbf{c^s_{min,I}}$ (Mole Fraction)	$\mathbf{k^s_{T,I}}$ $(J/K/m^3)$	$\mathbf{T^s_{min}}$ (K)	$\mathbf{g^s_{min,I}}$ (J/m^3)	$\mathbf{k^l_{b,I}}$ (J/m^3)	$\mathbf{c^l_{min,I}}$ (Mole Fraction)	$\mathbf{k^l_{T,I}}$ $(J/K/m^3)$	$\mathbf{T^l_{min}}$ (K)	$\mathbf{g^l_{min,I}}$ (J/m^3)
Hf	1.30×10^{9}	3.44×10^{-2}	1.54×10^{7}	1.44×10^{5}	-6.48×10^{11}	1.15×10^{9}	5.48×10^{-2}	1.84×10^{9}	2.97×10^{3}	-1.94×10^{10}
Ta	5.94×10^{8}	6.12×10^{-2}	1.54×10^{7}	1.44×10^{5}	-6.48×10^{11}	6.29×10^{8}	6.02×10^{-2}	1.54×10^{7}	1.44×10^{5}	-6.49×10^{11}
Ti	7.15×10^{8}	4.82×10^{-2}	1.53×10^{7}	1.44×10^{5}	-6.51×10^{11}	7.27×10^{8}	5.09×10^{-2}	1.54×10^{7}	1.44×10^{5}	-6.49×10^{11}
W	1.31×10^{8}	1.98×10^{-2}	1.54×10^{7}	1.44×10^{5}	-6.49×10^{11}	1.31×10^{8}	6.01×10^{-2}	1.54×10^{7}	1.44×10^{5}	-6.54×10^{10}

B.2. Normalised

Table B.10: Normalised interface properties of CM247 at a temperature T_0 of $1663K$.

Property	Value	Description
V_m	1	Molar Volume
ε	0.02	Gradient Energy Coefficient
L	33.33	Allen-Cahn Mobility
m	10	Double-well Height
T_0	0	Reference Temperature

Table B.11: Thermodynamic data obtained from ThermoCalc for CM247LC at a temperature T_0 of 1663 K.

Property	Value		Description
	Solid	Liquid	
S	26.8	29.8	Entropy Density
C_p	21.2	39.4	Specific heat capacity
D_{Hf}	4.92×10^{-4}	0.823	
D_{Ta}	1.40×10^{-5}	0.823	
D_{Ti}	4.04×10^{-5}	0.823	
D_{W}	1.49×10^{-7}	0.451	Element tracer self-diffusivities

Table B.12: Normalised parameters of the fitted paraboloid for solid and liquid phases after translation to equilibrium compositions, including thermal contributions.

	Solid Phase					Liquid Phase				
Element	$\mathbf{k^{s*}_{b,I}}$	$\mathbf{c^{s*}_{min,I}}$	$\mathbf{k^{s*}_{T,I}}$	$\mathbf{T^{s*}_{min}}$	$\mathbf{g^{s*}_{min,I}}$	$\mathbf{k^{l*}_{b,I}}$	$\mathbf{c^{l*}_{min,I}}$	$\mathbf{k^{l*}_{T,I}}$	$\mathbf{T^{l*}_{min}}$	$\mathbf{g^{l*}_{min,I}}$
Hf	70	0.69	0.83	2.9×10^{2}	-3.5×10^{4}	62	1.1	99	3.2	-1.0×10^{3}
Ta	32	1.2	0.83	2.9×10^{2}	-3.5×10^{4}	34	1.2	0.83	2.9×10^{2}	-3.5×10^{4}
Ti	38	0.96	0.82	2.9×10^{2}	-3.5×10^{4}	39	1.0	0.83	2.9×10^{2}	-3.5×10^{4}
W	7	0.40	0.83	2.9×10^{2}	-3.5×10^{4}	7.0	0.060	0.83	2.9×10^{2}	-3.5×10^{4}

C. Nanopore Identification

The aim of this paper is to demonstrate the effect of processing conditions on the nanopores formed during solidification. Therefore, the ability to identify the pores and to characterise them is necessary. This was performed with the help of the OpenCV library using the procedure outlined in Algorithm 1.

Algorithm 1 Pseudocode summarising how an image containing solidification pores is analysed to determine the distribution and size of the pores.

Input: Image I
Output: Contour data D
$I_{gray} \leftarrow$ convert_to_grayscale(I) ▷ Thresholding only done on grayscale images
$I_{thresh} \leftarrow$ apply_threshold$(I_{gray}$, threshold_value$)$ ▷ Threshold pixel value must be surpassed to label as solid.
$contours \leftarrow$ find_contours(I_{thresh})
$D \leftarrow$ initialize_empty_list$()$
for each $contour$ in $contours$ **do**
    $location \leftarrow$ get_location$(contour)$
    $size \leftarrow$ get_size$(contour)$
    D.append$((location, size))$
end for
save_contour_data(D, 'contour_data.txt')

The method starts with a thresholding operation to convert the data into liquid-constituted region and solid-constituted region. The former essentially represents pockets of highly concentrated material, which is what is referred to here in this paper as nanopores. After that, a contouring algorithm is used to segregate the two regions. To avoid fallacious contours from being generated by the algorithm, it is filtered to exclude the domain's boundaries and very large structures that it may be able to enclose.

D. Antitrapping Factor Derivation

This section presents an asymptotic analysis in the thin-interface limit as described in the introduction. The main objective of this section is to explain the origin of the artificial solute trapping, and then to show how specifying a suitable function as a pre-factor to the antitrapping current can eliminate this known spurious effect.

D.1. Sharp Interface Model

Only a single condition is needed to demonstrate artificial solute trapping - and to later eliminate it. This condition is shown in Equation D.1, which requires the chemical potential on the left-hand side of the interface to be equal to the chemical potential on the right-hand side. In short, this requires the chemical potential to be continuous through the thickness of the interface.

$$\mu_i|^+ = \mu_i|^- \tag{D.1}$$

D.2. Phase-Field

The phase-field formulation used throughout this work is based on the multi-component, multi-order-parameter grand-potential formulation of Aagesen et al. [20], introduced in Section 2.2. In its most general form, this framework assigns an independent order parameter ($\eta_{\alpha i}$) to each phase (α) and to each crystallographic orientation (i), with the liquid treated on the same footing as the solid phases. For the asymptotic analysis presented in this appendix, we reduce this general formulation. Specifically,

- a binary solid-liquid system,
- a single solid orientation, and
- the standard phase-fraction constraint [$\eta_s + \eta_l = 1$]

Under these assumptions, the liquid order parameter is not independent and can be written as ($\eta_l = 1 - \eta$), where ($\eta \equiv \eta_s$). Consequently, the governing equations

reduce to a single-order-parameter description that is mathematically consistent with — but simpler than — the general formulation used in the main text. All expressions derived below should therefore be interpreted as results for this specialised binary limit of the Aagesen model.

With this reduction in place, the grand-potential functional takes the form

$$\Omega = \int_V \left[\frac{1}{2}\kappa^2 |\nabla \eta|^2 + \omega_{mw}(\eta) + \omega_{th}(\eta, \mu, T) \right] dV \tag{D.2}$$

The three components of the energy functional Ω are shown in Equation D.2. The phase-field gradient captures the interfacial energy contribution. The second contribution ω_{mw} is the multi-well function. The multi-well function in Equation D.3 is for the most general system with N phases and multiple crystallographic orientations for each phase. The m constant is the height of the multiwell function. The subscript i in the energy definition refers to a chemical constituent of the system.

$$\omega_{mw} = m \left[\sum_{\alpha=1}^{N} \sum_{i=1}^{p_\alpha} \left(\frac{\eta_{\alpha i}^4}{4} - \frac{\eta_{\alpha i}^2}{2} \right) + \sum_{\alpha=1}^{N} \sum_{i=1}^{p_\alpha} \sum_{\beta=1}^{N} \sum_{j=1, \alpha i \neq \beta j}^{p_\beta} \frac{\Upsilon_{\alpha i \beta j}(\theta)}{2} \eta_{\alpha i}^2 \eta_{\beta j}^2 + \frac{1}{4} \right] \tag{D.3}$$

For a binary case the multiwell energy function reduces to that shown in Equation D.4. The multiwell energy function has minima at $\eta = 0$ and $\eta = 1$, which correspond to the liquid and solid phases, respectively. The anisotropy of the solid is assumed to be weak, so an isotropic interface ($\Upsilon_{\alpha i \beta j}(\theta) = \Upsilon(\theta) = \frac{3}{2}$) is assumed for the asymptotic analysis, which simplifies the expression considerably to that shown in Equation D.5. The subscript of $\Upsilon_{\alpha i \beta j}(\theta)$ is removed since the analysis in this section is for solid-liquid mixture with a single crystal orientation for the solid. This is reflected in all the relevant factors or functions in this section. Notice that $\Upsilon(\theta)$ is a dimensionless number that is related to the interfacial energy at

steady-state. This is explored in Appendix E.

$$\omega_{mw}(\eta) = m\left[\frac{\eta^4}{4} - \frac{\eta^2}{2} + \Upsilon(\theta)\eta^2(1-\eta)^2 + \frac{(1-\eta)^4}{4} - \frac{(1-\eta)^2}{2} + \frac{1}{4}\right] \quad \text{(D.4)}$$

$$\omega_{\text{mw}} = 2m\eta^2(1-\eta)^2 \quad \text{(D.5)}$$

The final contribution to the energy functional Ω is the grand potential energy. The grand potential was considered appropriate to use in this functional because solidification is done under constant pressure with a constant number of moles. The grand potential is given by the Legendre transform of the Helmholtz free energy and is shown below in Equation D.6 for a single phase α. Notice that f_α is the Helmholtz free energy.

$$\omega_{th,\alpha}(\mu, T) = f_\alpha - \sum_i \mu_i c_i^\alpha \quad \text{(D.6)}$$

The grand potential for any point in the domain is given by the sum shown in Equation D.7. The h_α function is an interpolation function that is dependent on the phase-field parameter. Notice that the only requirement of h_α at this stage is that it should be equal to one in phase α and zero in all other phases. In the case of a binary solid-liquid system, $h_s(\eta)$ is equal to one in the solid and zero in the liquid.

$$\omega_{th} = \sum_\alpha h_\alpha(\eta)\omega_{th,\alpha} \quad \text{(D.7)}$$

The evolution equations for the phase-field and the solute can now be written down as shown in Equations D.8 and D.9. Ω in Equations D.8 and D.9 refers to the energy functional's value in Equation D.2.

$$\frac{\partial \eta}{\partial t} = -L\frac{\delta \Omega}{\delta \eta} = -L\left(\frac{\partial \omega_{th}}{\partial \eta} + \frac{\partial \omega_{mw}}{\partial \eta} - \kappa^2 \nabla^2 \eta\right) \tag{D.8}$$

$$\frac{\partial c_i}{\partial t} = \nabla \cdot \left(M_i \nabla \frac{\delta \Omega}{\delta c_i}\right) = \nabla \cdot \left(M_i \nabla \frac{\partial \omega_{th}}{\partial c_i}\right) \tag{D.9}$$

The mobility M_i is a function of the order parameter and lies between the mobility of the solid and the liquid. This is shown in the following expressions. Notice that the chemical potential is assumed to be equal for all phases at any particular point, hence μ_i^α simply equals μ_i.

$$M_i = \sum_\alpha g_\alpha M_i^\alpha \tag{D.10}$$

$$M_i^\alpha = D_i^\alpha \frac{\partial c_i^\alpha}{\partial \mu_i} \tag{D.11}$$

A further modification will be made to the solute transport equation through the introduction of the antitrapping current. The antitrapping current is given by the expression in Equation D.12, and the modified solute transport equation is given by Equation D.13

$$\vec{J}_A^I = -s(\eta)\lambda[c_l - c_s]\frac{\partial \eta}{\partial t}\frac{\nabla \eta}{|\nabla \eta|} \tag{D.12}$$

$$\frac{\partial c_i}{\partial t} = \nabla \cdot \left(M_i \nabla \frac{\partial \omega_{th}}{\partial c_i} - \vec{J}_A^I\right) \tag{D.13}$$

The function $s(\eta)$ in the antitrapping current will prove to be necessary to eliminate the chemical potential's discontinuity at the interface.

D.3. Non-dimensionalisation

The aim of the non-dimensionalisation is to uncover a small parameter in the system of equations, which will allow for an asymptotic analysis to be performed. Before proceeding with the non-dimensionalisation, a relationship is needed for the gradient energy coefficient κ and the multi-well energy barrier height m will be written down. Those relationships are written down in Equations D.14 and D.15 respectively. The parameter σ is the interfacial energy and λ is the interface thickness in the phase-field model. These equations linking the phase-field parameters to physical ones are fairly ubiquitous in the phase-field literature and are derived based on a constant interfacial energy and specified interfacial width [27, 55].

$$\kappa^2 = \frac{3}{4}\lambda\sigma \tag{D.14}$$

$$m = 6\frac{\sigma}{\lambda} \tag{D.15}$$

On substitution into the phase-field evolution equation, we obtain Equation D.16.

$$\frac{\partial\eta}{\partial t} = -L\left[\frac{\partial\omega_{th}}{\partial\eta} + 6\frac{\sigma}{\lambda}\frac{\partial\omega_{mw}/m}{\partial\eta} - \frac{3}{4}\lambda\sigma\nabla^2\eta\right] \tag{D.16}$$

Next, we state the characteristic time, length, and energy scales where d_0 represents the capillary length and D_l the liquid diffusivity.

$$l^* = d_0 \tag{D.17}$$

$$t^* = \frac{d_0^2}{D_l} \tag{D.18}$$

$$f^* = \frac{\sigma}{d_0} \tag{D.19}$$

The dimensionless expressions for the phase-field parameter's evolution and for the concentration's evolution are shown in Equations D.20 and D.21, respectively. To avoid the overuse of notation in the coming sections, all equations from this point onwards are dimensionless, although the variables will not be given separate notation compared the preceding (dimensional) equations. The dimensionless relaxation constant τ is defined as $\frac{D}{\lambda L d_0}$. The parameter ε is assumed to be much smaller than one ($\varepsilon << 1$). Physically, this means that the interface width is much smaller than the capillary length of the system. Notice that in the remainder of the analysis, the system is assumed to be for a binary alloy with a diagonal Onsager matrix. The i subscript will therefore be dropped.

$$\tau\varepsilon^2\frac{\partial\eta}{\partial t} = \frac{3}{4}\varepsilon^2\nabla^2\eta - 6\frac{\partial\omega_{mw}}{\partial\eta} - \varepsilon\frac{\partial\omega_{th}}{\partial\eta} \tag{D.20}$$

$$\frac{\partial c}{\partial t} = \nabla\cdot\left(\frac{M}{D_l}\nabla\mu + s(\eta)\varepsilon[c_l - c_s]\frac{\partial\eta}{\partial t}\frac{\nabla\eta}{|\nabla\eta|}\right) \tag{D.21}$$

For simplicity, it will be assumed that D_s is much smaller than the liquid diffusivity D_l and can therefore be ignored. This gives Equation D.22

$$\frac{\partial c}{\partial t} = \nabla\cdot\left(\frac{\partial c_i^l}{\partial\mu}g_l(\eta)\nabla\mu + s(\eta)\varepsilon[c_l - c_s]\frac{\partial\eta}{\partial t}\frac{\nabla\eta}{|\nabla\eta|}\right) \tag{D.22}$$

The dimensionless phase-field evolution equation can be simplified further by assuming that the system exists around equilibrium. An expansion of the grand potential energy of each of the phases is given as follows:

$$\omega_{th,s}(\mu,T) = \omega_{th,s}(\mu_{,\mathrm{eq}},T) + \frac{\partial\omega_{th,s}}{\partial\mu}(\mu - \mu_{,\mathrm{eq}}) + \mathscr{O}(\delta\mu^2) \tag{D.23}$$

$$\omega_{th,l}(\mu,T) = \omega_{th,l}(\mu_{,\mathrm{eq}},T) + \frac{\partial\omega_{th,l}}{\partial\mu}(\mu - \mu_{,\mathrm{eq}}) + \mathscr{O}(\delta\mu^2) \tag{D.24}$$

Writing $\frac{\partial \omega_{th}}{\partial \eta}$ explicitly, we obtain the following expression in terms of interpolation functions' derivatives:

$$\frac{\partial \omega_{th}}{\partial \eta} = \frac{\partial h_s}{\partial \eta}(\omega_{th_s} - \omega_{th,l}) \tag{D.25}$$

$$= \frac{\partial h_s}{\partial \eta}\left(\frac{\partial \omega_{th,s}}{\partial \mu} - \frac{\partial \omega_{th,l}}{\partial \mu}\right)(\mu - \mu_{\text{eq}}) \tag{D.26}$$

We can make a further simplification using the Legendre transform linking the grand potential to the Helmholtz energy. This is illustrated below:

$$f_s(c_i, T) = \omega_{th,s}(\mu, T) - \frac{\partial \omega_{th,s}(\mu, T)}{\partial \mu}\mu \tag{D.27}$$

$$f_s(c, T) = f_s(c, T) - \frac{\partial f_s(c, T)}{\partial c}c - \frac{\partial \omega_{th,s}(\mu, T)}{\partial \mu}\mu \tag{D.28}$$

Given that the derivative of the Helmholtz energy with respect to the concentration is the chemical potential, we compare the terms in the latter expression to get the relation that:

$$\frac{\partial \omega_{th,s}(\mu_1, \mu_2, ..., \mu_N, T)}{\partial \mu_i} = -c_i \tag{D.29}$$

$$\frac{\partial h_s}{\partial \eta}\left(\frac{\partial \omega_{th,s}}{\partial \mu} - \frac{\partial \omega_{th,l}}{\partial \mu}\right)(\mu - \mu_{\text{eq}}) = \frac{\partial h_s}{\partial \eta}\left(c_{l,i}^{\text{eq}} - c_{s,i}^{\text{eq}}\right)(\mu - \mu_{\text{eq}}) \tag{D.30}$$

This returns the form of the dimensionless phase-field evolution equation that is shown below in Equation D.31.

$$\tau\varepsilon^2\frac{\partial \eta}{\partial t} = \frac{3}{4}\varepsilon^2\nabla^2\eta - 6\frac{\partial \omega_{\text{mw}}}{\partial \eta} - \varepsilon\frac{\partial h_s}{\partial \eta}\left(c_{l,i}^{\text{eq}} - c_{s,i}^{\text{eq}}\right)(\mu - \mu_{\text{eq}}) \tag{D.31}$$

Finally, the derivative of the concentration field will be converted to a derivative of the chemical potential. This is done by first recognizing that the composition can be written using the same interpolation function as the grand potential. This is shown below:

$$c = \sum_{\alpha} h_{\alpha} c^{\alpha} \tag{D.32}$$

By the product rule, we get the following:

$$\frac{\partial c}{\partial t} = \sum_{\alpha} \left[\frac{\partial h_{\alpha}}{\partial t} c^{\alpha} + \frac{\partial c^{\alpha}}{\partial t} h_{\alpha} \right] \tag{D.33}$$

Since the concentration in any phase is a function of the chemical potential, we can rewrite the $\frac{\partial c^{\alpha}}{\partial t}$ derivative using the chain rule as shown below.

$$\frac{\partial c}{\partial t} = \sum_{\alpha} \left[\frac{\partial h_{\alpha}}{\partial t} c^{\alpha} + \frac{\partial c^{\alpha}}{\partial \mu} \frac{\partial \mu}{\partial t} h_{\alpha} \right] \tag{D.34}$$

Finally, the dimensionless equation for the evolution of the concentration field is given by the following equation, where the chemical potential is now a dependent variable as well.

$$\begin{aligned} \frac{\partial \mu}{\partial t} \left(\frac{\partial c_l}{\partial \mu} h_l + \frac{\partial c_s}{\partial \mu} h_s \right) = \nabla \cdot \left(\frac{\partial c_l}{\partial \mu} g_l(\eta) \nabla \mu \right) + \\ \nabla \cdot \left(s(\eta) \varepsilon \left[c_l - c_s \right] \frac{\partial \eta}{\partial t} \frac{\nabla \eta}{|\nabla \eta|} \right) + \frac{\partial h_s}{\partial t} \left(c_l - c_s \right) \end{aligned} \tag{D.35}$$

D.4. Asymptotic Analysis

The dimensionless evolution equations developed in the preceding section are summarised below in Equations D.36 and D.37 for a 1D case moving with a local

interface velocity of v. Notice that the time derivatives $\frac{d}{dt}$ have been transformed into a velocity times a spatial gradient $-v\frac{d}{dx}$.

$$-\tau v\varepsilon^2\frac{d\eta}{dx} = \frac{3}{4}\varepsilon^2\frac{d^2\eta}{dx^2} - 6\frac{d\omega_{\mathrm{mw}}}{d\eta} - \varepsilon\frac{dh_s}{d\eta}\left(c_l^{\mathrm{eq}} - c_s^{\mathrm{eq}}\right)(\mu - \mu_{\mathrm{eq}}) \tag{D.36}$$

$$\begin{aligned} -v\frac{d\mu}{dx}\left(\frac{\partial c_l}{\partial\mu}h_l + \frac{\partial c_s}{\partial\mu}h_s\right) = \frac{d}{dx}\left(\frac{\partial c_l}{\partial\mu}g_l(\eta)\frac{d\mu}{dx}\right) - \\ \frac{d}{dx}\left(s(\eta)v\varepsilon\left[c_l - c_s\right]\frac{d\eta}{dx}\right) - v\frac{dh_s}{dx}\left(c_l - c_s\right) \end{aligned} \tag{D.37}$$

To perform the asymptotic analysis, we consider the inner and outer solutions with respect the interfacial region. The idea is that in the outer region, the influence of the interface is negligible since ε is a very small parameter. The outer solution, which is written with a tilde symbol, is given by the asymptotic expansion in Equation D.38. The inner expansions are shown in Equation D.39.

$$\begin{aligned} \tilde{\eta} &= \tilde{\eta}_0 + \varepsilon\tilde{\eta}_1 + \varepsilon^2\tilde{\eta}_2 + \mathscr{O}(\varepsilon^3) \\ \tilde{c} &= \tilde{c}_0 + \varepsilon\tilde{c}_1 + \varepsilon^2\tilde{c}_2 + \mathscr{O}(\varepsilon^3) \end{aligned} \tag{D.38}$$

$$\begin{aligned} \eta &= \eta_0 + \varepsilon\eta_1 + \varepsilon^2\eta_2 + \mathscr{O}(\varepsilon^3) \\ c &= c_0 + \varepsilon c_1 + \varepsilon^2 c_2 + \mathscr{O}(\varepsilon^3) \end{aligned} \tag{D.39}$$

For further clarity, the inner and outer regions are highlighted in Figure D.22.

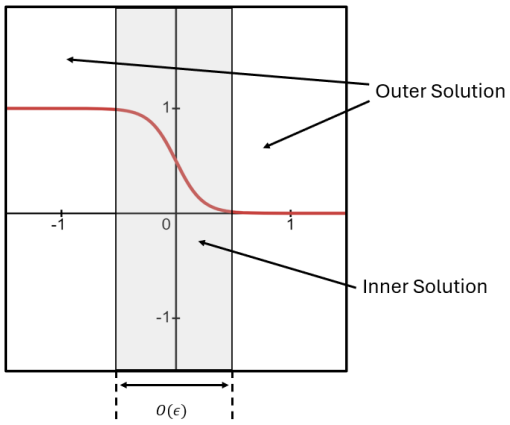

Figure D.22: The inner solution and the outer solutions. In this case there are two outer solutions because the region of rapid change is sandwiched between two bulk phases.

D.5. Outer Solution

First we will solve for the outer solution. When the asymptotic expansion expression is substituted into the phase-field evolution equation, it is quickly seen that all terms except $\tilde{\eta}_0$ are identically zero. For illustration, the outer solution is obtained only at leading order. The leading-order equation to solve is given in Equation D.40. This is done by taking the limit $x \to \pm\infty$, where $\tilde{\eta}_0$ assumes a value of either zero or one. This condition - in the bulk phase regions - is only satisfied if $\eta = 0$ or $\eta = 1$.

$$6\frac{\partial \omega_{mw}}{\partial \eta}|_{\tilde{\eta}_0} = 0 \tag{D.40}$$

More interestingly, the concentration equation for every order j in the outer region is simply the diffusion equation in the liquid region and a constant concentration in the solid region. This is given by Equations D.41 and D.42 respectively. The boundary conditions, however, for each order will be different.

$$\frac{\partial \tilde{\mu}_j}{\partial t} = \nabla^2 \tilde{\mu}_j \tag{D.41}$$

$$\frac{\partial \tilde{\mu}_j}{\partial t} = 0 \tag{D.42}$$

Notice, however that we now require two boundary conditions for the outer solution and only have one boundary condition (on the liquid side of the domain). The second boundary condition comes from matching with the inner layer. Unlike the outer solution for the phase-field equation, finding the exact solution to leading and subsequent orders of the solute transportation equation will not be needed. This is because the expressed aim of this asymptotic analysis is to determine a *condition* for a continuous chemical potential across the interface.

Matching Conditions

Since in the thin interface limit $\varepsilon << 1$, this would imply that the highest order derivative in the phase-field and concentration evolution equations become vanishingly unimportant. This is not the case in the inner region, however, since over the inner layer the rate of change of either variables is considerably large. Hence, we need an alternative variable to define changes over this small scale. To that end, we will define $\xi = x/\varepsilon$, where x is the coordinate along the local normal to the moving interface. The problem has therefore, effectively, been reduced to a single dimension.

$$-\tau v \varepsilon \frac{d\eta}{d\xi} = \frac{3}{4}\frac{d^2\eta}{d\xi^2} - 6\frac{d\omega_{\mathrm{mw}}}{d\eta} - \varepsilon \frac{dh_s}{d\eta}\left(c_l^{\mathrm{eq}} - c_s^{\mathrm{eq}}\right)\left(\mu - \mu_{\mathrm{eq}}\right) \tag{D.43}$$

$$-\frac{v}{\varepsilon}\frac{d\mu}{d\xi}\left(\frac{\partial c_l}{\partial \mu}h_l+\frac{\partial c_s}{\partial \mu}h_s\right)=\frac{1}{\varepsilon^2}\frac{d}{d\xi}\left(\frac{\partial c_l}{\partial \mu}\frac{d\mu}{d\xi}\right)$$
$$-\frac{1}{\varepsilon}\frac{d}{d\xi}\left(s(\eta)v\left[c_l-c_s\right]\frac{d\eta}{d\xi}\right)-\frac{v}{\varepsilon}\frac{dh_s}{d\xi}\left(c_l-c_s\right) \tag{D.44}$$

To match the inner and outer solutions. Two classes of matching conditions are enforced: matching conditions for chemical potential values in the matching region; and matching conditions over the chemical potentials' gradients. The latter will be important for calculating the solute flux at the boundary and thereby correct for non-equilibrium effects.

$$\begin{aligned}\lim_{\xi\to\pm\infty}\mu_0&=\lim_{x\to 0^{\pm}}\tilde{\mu}_0\\ \lim_{\xi\to\pm\infty}\mu_1-\xi\frac{\partial\tilde{\mu}_0}{\partial x}|^{\pm}&=\lim_{x\to 0^{\pm}}\tilde{\mu}_1\\ \lim_{\xi\to\pm\infty}\mu_2-\xi\frac{\partial\tilde{\mu}_1}{\partial x}|^{\pm}-\frac{\xi^2}{2}\frac{\partial\tilde{\mu}_0}{\partial x}|^{\pm}&=\lim_{x\to 0^{\pm}}\tilde{\mu}_2\end{aligned} \tag{D.45}$$

The gradient-type matching conditions are based on simply taking the derivatives of the matching conditions above.

$$\begin{aligned}\lim_{\xi\to\pm\infty}\frac{\partial^2\mu_1}{\partial\xi^2}&=\lim_{x\to 0^{\pm}}\frac{\partial\mu_0}{\partial x}=0\\ \lim_{\xi\to\pm\infty}\frac{\partial\mu_1}{\partial\xi}&=\lim_{x\to 0^{\pm}}\frac{\partial\tilde{\mu}_0}{\partial x}\\ \lim_{\xi\to\pm\infty}\frac{\partial\mu_1}{\partial\xi}-\xi\frac{\partial^2\tilde{\mu}_0}{\partial x^2}|^{\pm}&=\lim_{x\to 0^{\pm}}\frac{\partial\tilde{\mu}_1}{\partial x}\end{aligned} \tag{D.46}$$

Inner Solution

To obtain the inner solution, we will begin by substituting the asymptotic expression expansion of η into the dimensionless evolution equation for the inner solution (Equation D.43). This gives, to leading order, Equation D.47.

$$\frac{3}{4}\frac{d^2\eta_0}{d\xi^2} - 6\frac{d\omega_{\text{mw}}}{d\eta_0} = 0 \tag{D.47}$$

Multiplying through by $\frac{d\eta_0}{d\xi}$ and integrating once, we get an expression for the derivative of leading order term in the phase-field equation's expansion. The constant of integration is found to be zero by enforcing the boundary condition at $\xi = \pm\infty$. This gives us Equations D.48.

$$\left(\frac{d\eta_0}{d\xi}\right)^2 = 16\omega_{\text{mw}} \tag{D.48}$$

By substituting in the expression for the multi-well energy function in Equation D.4, we determine the expression for the derivative, which can be integrated to give a hyperbolic tangent function.

$$\frac{d\eta_0}{d\xi} = 4\sqrt{2}\eta_0(1-\eta_0) \tag{D.49}$$

$$\eta_0 = \frac{1}{2}\left[1 - \tanh\left(\frac{\xi}{8}\right)\right] \tag{D.50}$$

Similarly by substituting $\mu = \mu_0 + \varepsilon\mu_1 + \varepsilon^2\mu_2$ into the solute conservation equation and collecting leading order terms, we obtain the following relation.

$$\frac{d}{d\xi}\left(\frac{\partial c_l}{\partial \mu} g_l(\eta_0)\frac{d\mu_0}{d\xi}\right) = 0 \tag{D.51}$$

By integrating once, we obtain a constant of integration. This constant, A can be found by considering the value of the derivative as the ξ coordinate goes to infinity. Hence, $A = 0$.

$$\lim_{\xi \to \pm\infty} \frac{\partial c_l}{\partial \mu} \frac{d\mu_0}{d\xi} = A \tag{D.52}$$

$$\mu_0 = \bar{\mu}_0 \tag{D.53}$$

Since we don't have another boundary condition to solve for $\bar{\mu}_0$, we will use a solvability condition to determine its value. To determine this solvability condition, we will first take the derivative of Equation D.47 with respect to ξ, which will result in the following relationship.

$$\begin{aligned} \mathscr{L}\left(\frac{\partial \eta_0}{\partial \xi}\right) &= 0 \\ \mathscr{L} = \frac{3}{4}\frac{\partial^2}{\partial \xi^2} - 6\frac{\partial^2 \omega_{\mathrm{mw}}(\eta_0)}{\partial \eta^2} & \end{aligned} \tag{D.54}$$

To produce the solvability condition, we first need to write the phase-field evolution equation at first order $\mathscr{O}(\varepsilon)$. It can be shown by simple substitution that the equation at first order is given by Equation D.55.

$$\mathscr{L}\eta_1 = -\tau v \frac{d\eta}{d\xi} + \frac{dh_s}{d\eta}\left(c_l^{\mathrm{eq}} - c_s^{\mathrm{eq}}\right)(\mu - \mu_{\mathrm{eq}}) \tag{D.55}$$

The solvability condition is determined here by recognising the $\mathscr{L}$ operator is symmetric and linear. This means that it is a self-adjoint operator. This allows us to equate the inner products shown in Equation D.56.

$$\left(\mathscr{L}\frac{\partial \eta_0}{\partial \xi}, \eta_1\right) = \left(\mathscr{L}\eta_1, \frac{\partial \eta_0}{\partial \xi}\right) \tag{D.56}$$

This results in the condition shown in Equation D.57, which we can use to find $\bar{\mu}_0$. The expression for $\bar{\mu}_0$ is shown in Equation D.58. Also, since the leading order in the inner solution must approach the leading order in the outer solution (see matching conditions), $\tilde{\mu}_0 = \bar{\mu}_0$.

$$\int_{-\infty}^{\infty} \left[-\tau v \frac{d\eta_0}{d\xi} + \frac{dh_s}{d\eta}|_{\eta_0} \left(c_l^{\text{eq}} - c_s^{\text{eq}}\right) (\mu_0 - \mu_{\text{eq}}) \right] \frac{d\eta_0}{d\xi} d\xi = 0 \tag{D.57}$$

Notice that the expression for chemical potential essentially captures kinetic undercooling since the equilibrium chemical potential is controlled by the interface velocity. Dependence on the curvature of the interface can also be derived by treating a two-dimensional surface as shown by Echebarria et al. [27]. We have excluded the effect of curvature in this analysis, but it is shown in Section E that the Gibbs-Thomson relation is returned from performing an asymptotic expansion in the inner region of the interface.

$$\bar{\mu}_0 = \mu_{\text{eq}} - \frac{\sqrt{2}}{24} \frac{v\tau}{[c_l^{\text{eq}} - c_s^{\text{eq}}]} \tag{D.58}$$

Although the analysis to leading order permitted us to determine the leading order expressions exactly, this will not generally be possible for higher orders. That is not a concern here, however, since we are interested in the gradients at the interface rather than the exact expression at each order of the expansion. The $\mathscr{O}(\varepsilon^{-1})$ equation for chemical potential evolution is given by Equation D.59.

$$-v\frac{dh_s}{d\xi}(c_l-c_s)=\frac{d}{d\xi}\left(\frac{\partial c_l}{\partial\mu}g_l(\eta)\frac{d\mu_1}{d\xi}\right)+\frac{d}{d\xi}\left(s(\eta)v[c_l-c_s]\frac{d\eta}{d\xi}\right)$$
$$-v\frac{d\mu_0}{d\xi}\left(\frac{\partial c_l}{\partial\mu}h_l+\frac{\partial c_s}{\partial\mu}h_s\right) \quad \text{(D.59)}$$

Integrating the above equation once gives the following expression with a constant of integration B. Notice that the derivative of $\frac{d\mu_0}{d\xi}=0$.

$$-vh_s(c_l-c_s)=\frac{\partial c_l}{\partial\mu}g_l(\eta)\frac{d\mu_1}{d\xi}+s(\eta)v[c_l-c_s]\frac{d\eta_0}{d\xi}+B \quad \text{(D.60)}$$

To find the integration constant, we take the limit as ξ approaches $-\infty$, which gives us that $B=-v(c_l-c_s)$. On integrating again, we obtain an expression for the value of μ_1 in terms of a integrand $p(\eta_0)$ and a constant of integration $\bar{\mu}_1$. This is shown in Equation D.63.

$$\frac{d\mu_1}{d\xi}=\frac{v[c_l-c_s](h_s-1-s(\eta_0)\frac{d\eta_0}{d\xi})}{\frac{\partial c_l}{\partial\mu}g_l(\eta_0)} \quad \text{(D.61)}$$

$$p(\eta_0)=\frac{h_s-1-s(\eta_0)\frac{d\eta_0}{d\xi}}{\frac{\partial c_l}{\partial\mu}g_l(\eta_0)} \quad \text{(D.62)}$$

$$\mu_1=\bar{\mu}_1+v[c_l-c_s]\int_0^{\xi}p(\eta_0)d\xi \quad \text{(D.63)}$$

Finally, to calculate the antitrapping factor, we must eliminate the jump in chemical potential across the interface. This is done by enforcing $\lim_{\xi\to+\infty}\tilde{\mu}_1=\lim_{\xi\to-\infty}\tilde{\mu}_1$. To do so, we make use of the matching condition below.

$$\lim_{\xi \to \pm\infty} \mu_1 - \xi \frac{\partial \tilde{\mu}_0}{\partial x}|^{\pm} = \lim_{x \to 0^{\pm}} \tilde{\mu}_1 \tag{D.64}$$

Recognising that $\frac{\partial \mu_1}{\partial \xi} = \frac{\partial \tilde{\mu}_0}{\partial x}$, we determine that the chemical potential can be written as the following.

$$\tilde{\mu}_1|^{+} = \bar{\mu}_{1,i} + v[c^l - c^s] \int_0^{\infty} [p(\eta_0) + 1]\, d\xi \tag{D.65}$$

$$\tilde{\mu}_1|^{-} = \bar{\mu}_{1,i} + v[c^l - c^s] \int_0^{-\infty} p(\eta_0) d\xi \tag{D.66}$$

It is therefore clear from matching the chemical potential on both sides of the interface that the integral in Equations D.65 and D.66 must be equal. This results in the following condition.

$$\int_0^{\infty} [p(\eta_0) + 1]\, d\xi = \int_0^{-\infty} p(\eta_0) d\xi \tag{D.67}$$

The final step is to recognise that $p(\eta_0)$ is equal to zero at negative infinity and one at positive infinity. A function that satisfies those same properties is $p(\eta_0) = h_s(\eta_0) - 1$. This solution, however, is non-unique, and other valid functions conceivably exist. After some algebra, we obtain the form of the antitrapping pre-factor function $s(\eta_0)$ as shown in Equation D.68. Note the antitrapping factor is simply a combination of two interpolation functions and the leading order solution to the inner-boundary problem - all of which are explicitly known.

$$s(\eta_0) = -\frac{g_s(\eta_0)[1 - h_s(\eta_0)]}{\frac{d\eta_0}{d\xi}} \tag{D.68}$$

Extension to Multi-component Systems

If the analysis in this section is extended to multi-component alloys, then under the condition that the solute mobilities are dominated by self-diffusivities and not by cross-diffusivities, then N equations of the form of Equation D.59 would be obtained. As a result, the derivation of the chemical potential's derivative with respect to ξ would be repeated identically to give the same antitrapping factor $s(\eta_0)$ for each element. It is therefore concluded that this analysis is applicable to systems at high temperatures where the diffusion of individual species can be treated separately.

E. Gibbs-Thomson relation at the thin interface limit

This section briefly demonstrates how the grand potential-based model by Aagesen et al. [20] accounts for curvature-dependent capillarity in a form identical to the Gibbs-Thomson relation at the thin-interface limit. Equation E.1 is obtained from the non-dimensionalisation in Section D.3.

$$\tau\varepsilon^2\frac{\partial\eta}{\partial t} = \frac{3}{4}\varepsilon^2\nabla^2\eta - 6\frac{\partial\omega_{mw}}{\partial\eta} - \varepsilon\frac{\partial\omega_{th}}{\partial\eta} \tag{E.1}$$

The Laplacian operator can be written approximately near a surface as shown below in Equation E.2. We can then re-write Equation E.1 as shown in Equation E.3, where ω_{mw} is given by the expression in Equation E.4.

$$\nabla^2\eta = \frac{d^2\eta}{dn^2} + \kappa\frac{d\eta}{dn} + \mathscr{O}(1) \tag{E.2}$$

$$-v\tau\varepsilon^2\frac{d\eta}{dn} = \frac{3}{4}\varepsilon^2\left[\frac{d^2\eta}{dn^2} + \kappa\frac{d\eta}{dn}\right] - 6\frac{\partial\omega_{mw}}{\partial\eta} - \varepsilon\frac{\partial\omega_{th}}{\partial\eta} \tag{E.3}$$

$$\omega_{mw} = \left[\Upsilon(\theta) + \frac{1}{2}\right]\eta^2(1-\eta)^2 \tag{E.4}$$

If we now write $\xi = \frac{n}{\varepsilon}$ to scale the coordinate normal to the surface (n) by the small parameter ε, we end up with the differential equation in the inner region. Next, we would substitute the asymptotic expansion for the inner solution and write the equations for the leading and first orders, $\mathscr{O}(1)$ and $\mathscr{O}(\varepsilon)$, respectively.

$$-v\tau\varepsilon\frac{d\eta}{d\xi} = \frac{3}{4}\varepsilon^2\left[\frac{1}{\varepsilon^2}\frac{d^2\eta}{d\xi^2} + \frac{\kappa}{\varepsilon}\frac{d\eta}{d\xi}\right] - 6\frac{\partial\omega_{mw}}{\partial\eta} - \varepsilon\frac{dh_s}{d\eta}\left(c_l^{\mathrm{eq}} - c_s^{\mathrm{eq}}\right)(\mu - \mu_{\mathrm{eq}}) \quad \text{(E.5)}$$

At the leading order $\mathscr{O}(1)$, we can write Equation E.6, which leads to Equation E.7. By solving Equation E.7, we determine the solution for the leading-order of the phase-field order parameter η_0. Notice that $\Upsilon(\theta)$ is a dimensionless parameter that reflects the anisotropy of the multi-well energy term and should not be confused with the interfacial energy. $\Upsilon(\theta)$ is identical to $\Upsilon_{\alpha i\beta j}$ in the cross bulk term of the multiwell energy contribution ω_{mw}. However, the subscript is dropped since we are dealing with a binary alloy. The dependence on the orientation θ is written explicitly to highlight that $\Upsilon(\theta)$ is, in general, anisotropic.

$$\frac{3}{4}\frac{d^2\eta_0}{d\xi^2} - 6\frac{d\omega_{mw}(\eta_0)}{d\eta} = 0 \quad \text{(E.6)}$$

$$\left[\frac{3}{8}\left(\frac{d\eta_0}{d\xi}\right)^2 - 6\omega_{mw}\right]\frac{d\eta_0}{d\xi} = 0 \quad \text{(E.7)}$$

$$\frac{d\eta_0}{d\xi} = 4\sqrt{\left[\Upsilon(\theta) + \frac{1}{2}\right]}\eta(1-\eta) \quad \text{(E.8)}$$

$$\eta_0 = \frac{1}{2}\left[1 - \tanh\left(2\xi\sqrt{\Upsilon(\theta) + \frac{1}{2}}\right)\right] \quad \text{(E.9)}$$

If we repeat the same procedure for the first order $\mathscr{O}(\varepsilon)$ we obtain Equation E.10.

The differential operator $\mathscr{L}$ is given by Equation E.11.

$$\mathscr{L}\eta_1 = -\tau v\frac{d\eta_0}{d\xi} + \frac{3}{4}\kappa\frac{d\eta_0}{d\xi} + \frac{dh_s(\eta_0)}{d\eta}\left(c_l^{\mathrm{eq}} - c_s^{\mathrm{eq}}\right)(\mu - \mu_{\mathrm{eq}}) \tag{E.10}$$

$$\mathscr{L} = \frac{3}{4}\frac{\partial^2}{\partial\xi^2} - 6\frac{\partial^2\omega_{\mathrm{mw}}(\eta)}{\partial\eta^2} \tag{E.11}$$

Using the fact that $\mathscr{L}$ is linear and symmetric, we can use its self-adjoint property to relate the chemical potential on the right-hand side of Equation E.10 to the curvature. More specifically, we can write the following.

$$(\mathscr{L}\frac{d\eta_0}{d\xi}, \eta_1) = (\frac{d\eta_0}{d\xi}, \mathscr{L}\eta_1) \tag{E.12}$$

From Equation E.6, we can see that $\mathscr{L}\frac{d\eta_0}{d\xi}$ is equal to zero and hence,

$$\int_{-\infty}^{\infty}\frac{d\eta_0}{d\xi}\mathscr{L}\eta_1\, d\xi = 0. \tag{E.13}$$

This leads to the expression in Equation E.14, where all the definite integrals can be evaluated exactly. The values of these integrals are given in Equations E.15 and E.16. Notice that Equation E.16 implies that the surface energy is proportional to $\sqrt{\Upsilon(\theta) + \frac{1}{2}}$.

$$\begin{aligned} &-\tau v\int_{-\infty}^{\infty}\left(\frac{d\eta_0}{d\xi}\right)^2 d\xi + \frac{3}{4}\kappa\int_{-\infty}^{\infty}\left(\frac{d\eta_0}{d\xi}\right)^2 d\xi \\ &\quad + (c_l^{eq} - c_s^{eq})(\mu_0 - \mu_{eq})\int_{-\infty}^{\infty}\frac{d\eta_0}{d\xi}\frac{dh_s}{d\eta_0}d\xi = 0. \end{aligned} \tag{E.14}$$

$$\int_{-\infty}^{\infty} \frac{d\eta_0}{d\xi}\frac{dh_s}{d\eta_0}d\xi = h_s|_0^1 = 1 \tag{E.15}$$

$$\int_{-\infty}^{\infty} \left(\frac{d\eta_0}{d\xi}\right)^2 d\xi = \frac{2}{3}\sqrt{\Upsilon(\theta)+\frac{1}{2}} \tag{E.16}$$

Now, substituting these integrals into Equation E.14, returns Equation E.17. Equation E.17 therefore shows that this grand potential-based approach produces a reduction in chemical potential for a concave surface (+ve κ) and an increase in chemical potential for a convex surface (-ve κ).

$$\mu_{\text{eq}} + \frac{2\tau v\sqrt{\Upsilon(\theta)+\frac{1}{2}}}{3\Delta c} - \frac{\kappa\sqrt{\Upsilon(\theta)+\frac{1}{2}}}{2\Delta c} = \mu_0 \tag{E.17}$$

Ignoring the effect of kinetic undercooling, ($v = 0$), Equation E.17 reduces to the Gibbs–Thomson relation

$$\Delta\mu = -\frac{\kappa}{2\Delta c}\sqrt{\Upsilon(\theta)+\frac{1}{2}}. \tag{E.18}$$

To examine the anisotropy explicitly, we write

$$\Upsilon(\theta) = \Upsilon_0\left[1+\delta\cos\left(\frac{k}{2\pi}(\theta-\theta_0)\right)\right]. \tag{E.19}$$

Then

$$\begin{aligned}\sqrt{\Upsilon(\theta)+\frac{1}{2}} &= \sqrt{\Upsilon_0+\frac{1}{2}+\Upsilon_0\delta\cos\left(\frac{k}{2\pi}(\theta-\theta_0)\right)} \\ &= \sqrt{\Upsilon_0+\frac{1}{2}}\sqrt{1+\frac{\Upsilon_0}{\Upsilon_0+\frac{1}{2}}\delta\cos\left(\frac{k}{2\pi}(\theta-\theta_0)\right)} \\ &= \sqrt{\Upsilon_0+\frac{1}{2}}\left[1+\frac{\Upsilon_0}{2\Upsilon_0+1}\delta\cos\left(\frac{k}{2\pi}(\theta-\theta_0)\right)+\mathscr{O}(\delta^2)\right]. \quad \text{(E.20)}\end{aligned}$$

Substituting into Equation E.18 gives

$$\Delta\mu = -\frac{\sqrt{\Upsilon_0+\frac{1}{2}}}{2\Delta c}\kappa\left[1+\frac{\Upsilon_0}{2\Upsilon_0+1}\delta\cos\left(\frac{k}{2\pi}(\theta-\theta_0)\right)+\mathscr{O}(\delta^2)\right]. \quad \text{(E.21)}$$

Defining the effective isotropic capillary coefficient

$$\Gamma_0 = \frac{\sqrt{\Upsilon_0+\frac{1}{2}}}{2\Delta c}, \quad \text{(E.22)}$$

the Gibbs–Thomson relation becomes

$$\Delta\mu = -\Gamma_0\kappa\left[1+\frac{\Upsilon_0}{2\Upsilon_0+1}\delta\cos\left(\frac{k}{2\pi}(\theta-\theta_0)\right)+\mathscr{O}(\delta^2)\right]. \quad \text{(E.23)}$$

Equation E.23 is identical in structure to the classical sharp–interface Gibbs–Thomson condition,

$$\Delta\mu = -\Gamma_{\text{eff}}(\theta)\,\kappa, \quad \text{(E.24)}$$

with an effective orientation–dependent surface energy

$$\Gamma_{\text{eff}}(\theta) = \Gamma_0 \left[1 + \frac{\Upsilon_0}{2\Upsilon_0 + 1} \delta \cos\left(\frac{k}{2\pi} (\theta - \theta_0) \right) \right]. \tag{E.25}$$

Thus, in the thin–interface limit, the modified multi–well potential recovers the classical sharp–interface chemical potential drop with a weakly anisotropic surface energy, ensuring that the correct Wulff construction is obtained for $\delta \ll 1$.